



Healing of keyhole porosity by means of defocused laser beam remelting: *Operando* observation by X-ray imaging and acoustic emission-based detection

Charlotte de Formanoir^{a,*}, Milad Hamidi Nasab^a, Lucas Schlenger^a, Steven Van Petegem^b, Giulio Masinelli^c, Federica Marone^d, Antti Salminen^e, Ashish Ganvir^e, Kilian Wasmer^c, Roland E. Logé^a

^a Thermomechanical Metallurgy Laboratory – PX Group Chair, Ecole Polytechnique Fédérale de Lausanne (EPFL), CH-2002 Neuchâtel, Switzerland

^b Structure and Mechanics of Advanced Materials, Photon Science Division, Paul Scherrer Institut, PSI, Forschungsstrasse 111, 5232 Villigen, Switzerland

^c Laboratory for Advanced Materials Processing (LAMP), Swiss Federal Laboratories for Materials Science and Technology (Empa), CH-3602 Thun, Switzerland

^d TOMCAT, Photon Science Division, Paul Scherrer Institut, PSI, Forschungsstrasse 111, 5232 Villigen, Switzerland

^e Digital Manufacturing and Surface Engineering research group, Department of Mechanical and Materials Engineering, University of Turku, FI-20014, Finland

ARTICLE INFO

Keywords:

Laser Powder Bed Fusion
Acoustic emission
In-situ monitoring
Synchrotron X-ray imaging
Laser remelting

ABSTRACT

One of the remaining challenges in Laser Powder Bed Fusion (LPBF) of metals is the control of the formation of keyhole pores, resulting from a local excessive energy input during processing. Such defects can lead to degraded mechanical properties and are typically detected and/or removed after the process through non-destructive quality-inspection procedures and porosity-removal treatments. Monitoring and controlling the formation of defects during the LPBF process can allow circumventing such time-consuming and costly post-process stages. This paper develops a new approach to perform in-situ healing of deep keyhole pores, using a positively defocused laser beam with finely tuned laser remelting process parameters. Synchrotron radiographic images of the process zone are acquired during laser remelting. The use of *operando* imaging enables the visualization of pore removal during processing, and unveils the effect of various remelting conditions on the healing efficiency. The acoustic signals generated during laser remelting are recorded using a high-sensitivity optical microphone, and analyzed in parallel with the X-ray images, allowing the acoustic signature of defect healing to be identified. The present paper demonstrates for the first time that an airborne acoustic sensor can be used to monitor the healing of keyhole pores during LPBF.

1. Introduction

Laser Powder-Bed Fusion (LPBF) is an additive manufacturing (AM) process which relies on a laser to selectively melt successive layers of metallic powder based on a 3D CAD model [1,2]. LPBF enables the production of complex geometries while minimizing lead time and material waste. Despite its many advantages, the process still faces several limitations. In particular, the stochastic formation of defects remains a major issue as it leads to degraded mechanical properties [3–5], impeding broader industrialization of LPBF for critical applications. Defects in as-built LPBF parts can either be related to the powder feedstock (i.e. small spherical metallurgical pores originating from the transfer of entrapped inert gas inclusions from powder to the AM part

[6–9]) or to the laser-material interactions during processing [7,10–12]. The latter may induce various types of porosity, such as lack-of-fusion, keyhole and balling [13].

Pores are typically detected and characterized through time-consuming destructive or non-destructive post-process quality inspection procedures, such as microscopic cross-section analysis or X-ray Computed Tomography (CT) [14,15]. Additionally, Hot Isostatic Pressing (HIP) is routinely performed after LPBF to reduce porosity, by applying a high pressure and high temperature for an extended duration [16]. These post-process inspection techniques and treatments are expensive, time-consuming and present some limitations. For instance, gas-containing-pores may re-grow upon post-HIP exposure to high temperatures [8,17], negatively impacting the final mechanical

* Corresponding author.

E-mail address: charlottedeformanoir@hotmail.com (C. de Formanoir).

<https://doi.org/10.1016/j.addma.2023.103880>

Received 3 July 2023; Received in revised form 11 November 2023; Accepted 12 November 2023

Available online 16 November 2023

2214-8604/© 2023 The Authors. Published by Elsevier B.V. This is an open access article under the CC BY license (<http://creativecommons.org/licenses/by/4.0/>).

performance [10]. HIP is also inefficient for the removal of open pores. Such drawbacks highlight the importance of achieving fully dense parts during the process. In order to do so, it is critical to choose an adequate set of LPBF process parameters, which largely determines the geometry of the melt pool, its stability and the formation of lack-of-fusion and keyhole pores. It was demonstrated that normalized-enthalpy-based models can be used to predict the transition from conduction to keyhole melting mode [12,18], and thus to minimize porosity formation during AM processing.

Although process parameters optimization has been largely explored [11,14,19–21], a fully dense as-built material remains difficult to achieve. In particular, the keyhole melting mode is in terms of fatigue and pinning of these bubble upon solidification considered. A bulkier repeatability issues. one of the main contributors to the formation of porosity in LPBF parts [22–24]. This regime occurs when excessive energy density [25,26] induces rapid evaporation of the material. The resulting intense recoil pressure generates a deep and narrow, so-called “keyhole”, cavity [27]. As this keyhole collapses, gas bubbles are entrapped in the melt and are pinned upon solidification [19,22,28]. This results in the formation of porosity which can largely impact the final mechanical properties of the part [29,30], particularly in terms of fatigue resistance [5]. Hamidi et al. [31] recently reported the occurrence of stochastic instabilities leading to abrupt regime transitions and to the formation of keyhole pores under constant laser processing conditions. Such unpredictable defects can be caused by a multiplicity of factors (e.g. laser beam acceleration and deceleration at the beginning and end of the line track, presence of specific geometrical features, etc.) and cannot be systematically circumvented by the choice of processing window. To maximize the material's density, it is imperative to investigate how these pores can be removed during the process, rather than through post-treatments. Laser remelting (LR) – which consists in re-exposing an already scanned layer to the laser beam, without new powder being delivered – has been reported as a tool to densify LPBF parts [32–36]. When performed with parameters similar to those used during melting, it can successfully remove lack-of-fusion defects [32] or metallurgical pores located at relatively shallow depths ($\approx 50\ \mu\text{m}$ below the surface [36]). However, keyhole defects typically lie deeper underneath the surface, so that the penetration of the remelting pool may be insufficient to remove such pores [34,37]. Additionally, it is paramount to avoid the creation of new keyhole pores during the remelting routine, at the same depth or deeper than the original voids [37]. In order to achieve a sufficient remelting depth for healing to take place, while ensuring conduction mode to avoid the formation of new defects, the parameters that were used for melting of the defective layer cannot be re-iterated for the remelting cycle. In this context, the defocus of the laser beam can be used as an additional parametric degree of freedom and a tool towards better control of the melt pool dimensions and processing regime. Negative defocus (i.e. convergent beam) tends to favor the keyhole mode and associated porosity formation, while positive defocus (i.e. divergent beam) is more prone to induce a stable conduction regime [38,39]. By positively defocusing the beam and adjusting the laser power (or the scanning speed) such as to maintain an appropriate normalized enthalpy, larger and deeper melt pools can be generated, which gives more opportunity for gas bubbles to escape [40] while maintaining a conduction regime.

Ideally, to improve the reliability and robustness of the LPBF process, removal of defects through finely tuned remelting parameters must be combined with real-time process monitoring of defect formation and removal. This would allow not only to detect the occurrence of keyhole defect(s) and establish the need to perform local in-situ healing, but also to confirm that healing is properly done.

Various monitoring techniques for laser melting have been reported in the past decade. On the one hand, spatially integrated optical sensors such as photodiodes [41–43] and pyrometers [44–48] reduce the signal from the field of view down to a single and easy-to-process quantity, corresponding to the amount of light reaching the detector. Their low

cost, high sensitivity, robustness, and high data acquisition rates make them advantageous [49]. On the other hand, spatially resolved optical sensors such as infrared and high speed cameras allow the melt pool size, shape and temperature profiles to be measured [41,42,46,48,50]. However, this is achieved at the expense of sampling rate, cost, and data management, which can become challenging as the amount of collected data increases with the number of pixels) [49,51]. Furthermore, a significant limitation of optical methods is that they do not capture phenomena taking place underneath the surface, at the bottom of the melt pool or of the keyhole depression zone. Complementary to these optical techniques, acoustic emission (AE) analysis has been used as a low-cost and robust monitoring technique, providing information on the laser-material interactions occurring in the entire volume of material, instead of the top surface. Airborne acoustic signals are caused by gaseous pressure and shock waves generated in the vicinity of the melt pool. In other words, the more vapor or plasma generated in the process (i.e. by increasing the energy input or going from conduction to keyhole regime), the stronger the emitted airborne acoustic signal [31,52,53]. The analysis of AE signals was first performed in the context of laser welding. AE was identified as a valid technique for monitoring welding, allowing to differentiate between good and bad quality welds, to identify changes in the weld penetration depth and to distinguish keyhole from conduction mode [52–55]. In most studies, machine learning tools such as neural networks were used to classify welds on the basis of their AE signals. A similar approach is now increasingly adopted for the monitoring of AM. Several papers have demonstrated the ability to differentiate lack-of-fusion, conduction, stable and unstable keyhole regimes based on AE signal analysis [31,43,56–65]. Recently, Hamidi et al. [31] successfully showed that the acoustic information recorded from the laser-material interaction zone can be used to identify changes between conduction, stable and unstable keyhole regimes under constant laser processing conditions, with a very high confidence. However, to the best of our knowledge, airborne AE-based monitoring has never been used to detect the occurrence of porosity removal during LPBF. Shevchik et al. observed by means of X-ray imaging the surfacing and elimination of pores during laser welding. Such events were classified by a CNN, using both AE and optical signals, with a confidence level of 73%. However, rather than being intentionally triggered by specifically designing processing conditions prone to healing, these events were stochastically occurring in unstable keyhole mode [43].

The present paper aims at combining in-process control of the part quality (through laser remelting) with airborne AE-based monitoring. The acoustic signals generated during laser remelting are recorded using a high-sensitivity optical microphone while simultaneously acquiring radiographic images of the process zone. Synchrotron X-ray imaging is a powerful non-destructive technique for *operando* observation of the process, allowing to visualize sub-surface melt pool dynamics and to reveal the underlying physical phenomena occurring during LPBF. Features such as geometrical changes in the melt pool and depression zone, defect formation and by-product emission (e.g. spattering) can be documented, without interfering with the process [7,22,66–82]. Here, the AE signals are analyzed in parallel to the images acquired by X-ray radiography, in order to identify the acoustic signature of keyhole pore removal. The aim of the present paper is, thus, twofold.

A first objective is to develop a new strategy for the in-situ healing of pores and to implement it while performing *operando* X-ray imaging. X-ray imaging allows investigating the mechanisms of pore elimination when remelting with a defocused laser beam, and to evaluate the effect of key remelting parameters on healing efficiency.

A second objective is to demonstrate the potential of using AE to monitor the occurrence of defect healing during laser remelting. To that end, the AE signals are time-aligned with the X-ray images and analyzed to identify a potential acoustic signature for porosity healing. This paper therefore contributes to increasing the maturity of AE as a monitoring technique for LPBF, and this time without the need of Machine Learning (ML) algorithms.

Table 1

Chemical composition (in weight percent) of the 316 L powder feedstock.

Fe	Cr	Ni	Mo	C	Other
Balance	18	12	3	< 0.03	< 1.0

2. Materials and methods

2.1. Experimental set-up and processing conditions

A gas atomized 316 L stainless steel powder acquired from Oerlikon Metco, with the chemical composition listed in Table 1 and a particle size distribution ranging from 15 μm to 45 μm , was used in this study. The morphology of the powder was predominantly spherical with the

presence of sporadic satellites.

All experiments were carried out using a miniaturized LPBF device designed at the Paul Scherrer Institute (PSI) [83,84] (Fig. 1), which mimics a commercial LPBF machine while being optimized for in-situ X-ray measurements. Its relatively small dimensions (height: 520 mm, width and depth: 280 mm and 260 mm) and weight (25 kg) make it easily transportable to synchrotron beamlines. As illustrated in Fig. 1, the presence of two glassy carbon windows allows the X-ray beam to enter at the back (11) of the device, interact with the specimen (8) and exit at the front (4). The printing chamber contains a build plate of $12 \times 12 \text{ mm}^2$ (7). Prior to each recoating, the build plate is moved down by a height corresponding to one layer thickness (in this case 30 μm). The powder is delivered by gravity from a hopper-based delivery system (12), equipped with a doctor blade scrapping the excess powder on its

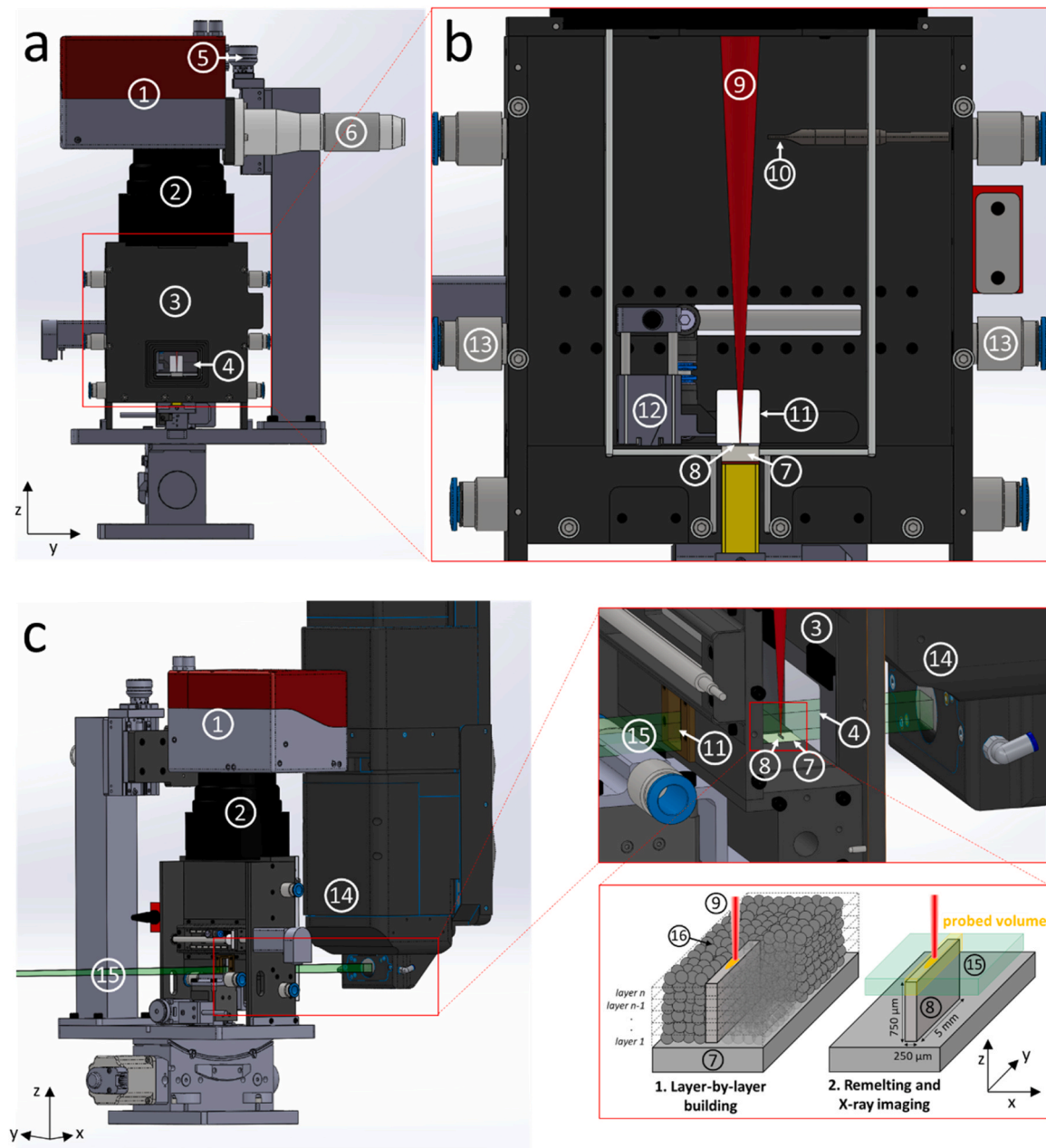


Fig. 1. Front view of the miniaturized LPBF device (a) with and (b) without the front door, side view of the device in operation at the TOMCAT beamline (c). 1) scanning head, 2) F-theta lens, 3) front door, 4) X-ray exit window, 5) vertical stage to adjust the focal length, 6) laser collimator, 7) build plate, 8) sample, 9) laser beam, 10) microphone, 11) X-ray entrance window, 12) powder hopper and recoater, 13) gas inlet (left) and outlet (right), 14) microscope, 15) X-ray beam, 16) powder bed.

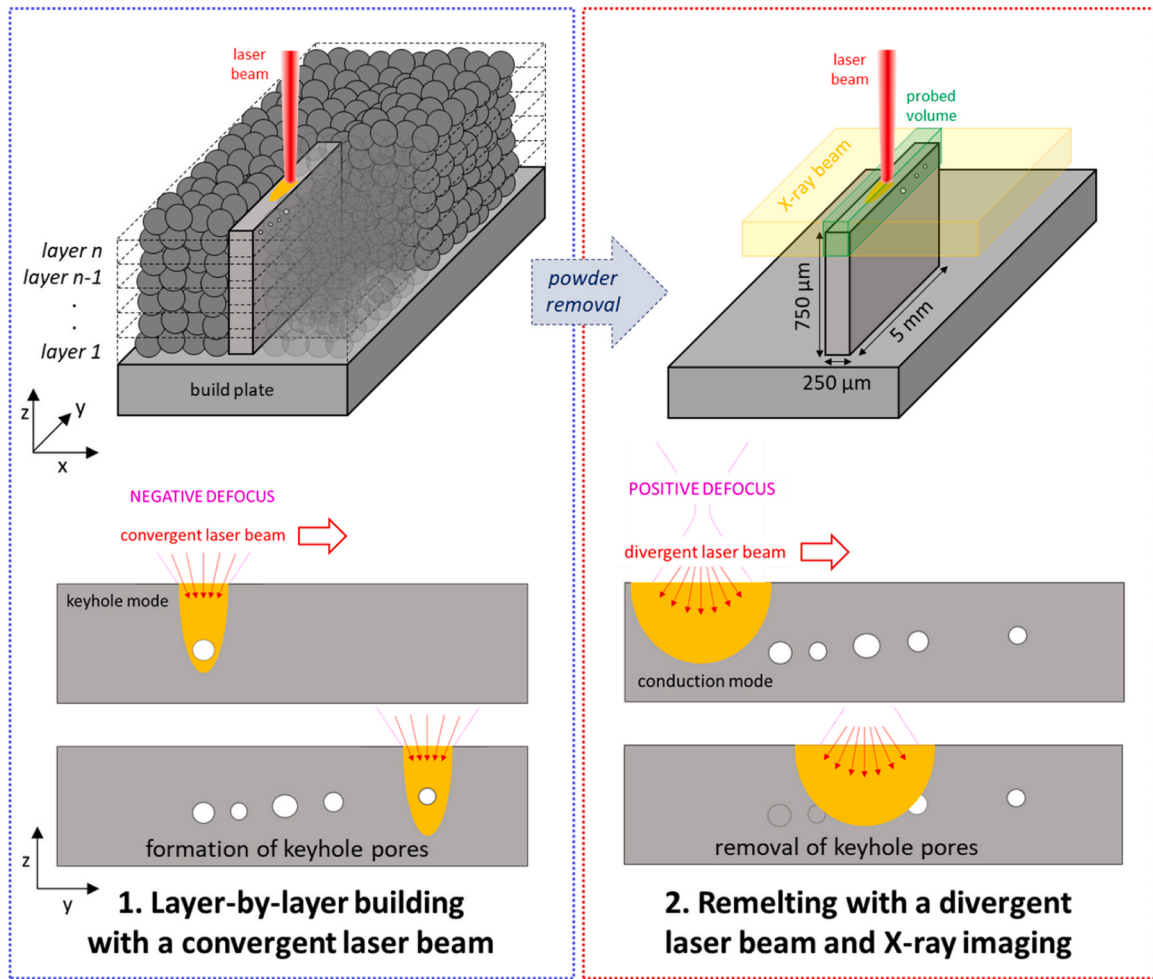


Fig. 2. Schematic view of the building of the wall in keyhole melting mode (on the left), and of the remelting of its top surface using a positively defocused laser beam, after removal of the surrounding powder (on the right). X-ray imaging of the top region of the wall allows the removal of keyhole pores to be visualized.

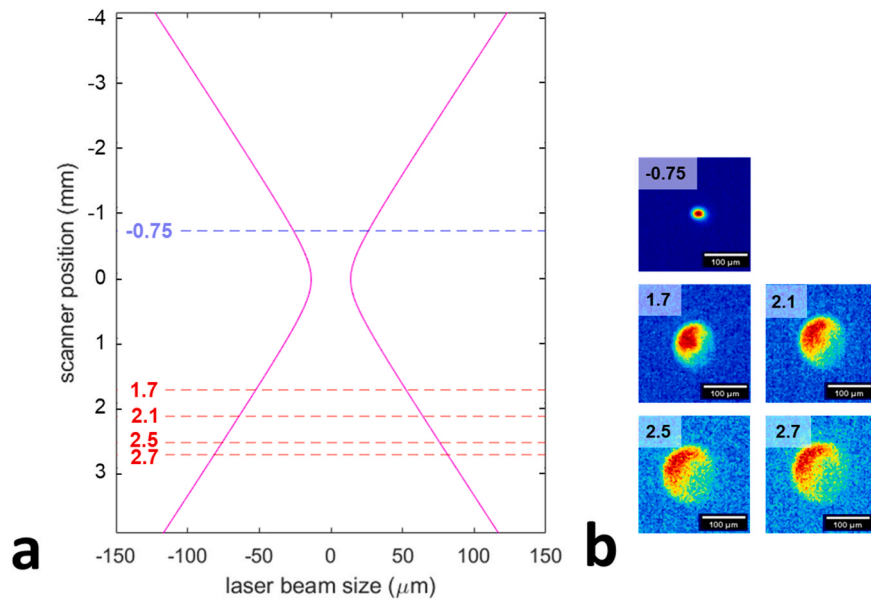


Fig. 3. a) Laser beam profile as calculated theoretically using Eq. 1, and b) as measured at the different scanner positions considered in the present work by the CCD camera-based beam profiler. As a result of small misalignment of the laser beam through the optical chain, a deviation from Gaussian profile was observed in both defocus directions.

Table 2

Process parameters for LPBF building of the walls in keyhole mode.

	Denomination	Power [W]	Speed [mm/s]	Hatch distance [μm]	Beam radius [μm]	Layer thickness [μm]	Normalized enthalpy
Building parameters	<i>B1</i>	130	280	40	22.5	30	50.4
	<i>B2</i>	150	280	40	22.5	30	58.1
	<i>B3</i>	120	280	40	22.5	30	46.5

Table 3

Process parameters for laser remelting.

	Denomination	Power [W]	Speed [mm/s]	Hatch distance [μm]	Number of remelting passes	Beam radius ω [μm]	Normalized enthalpy
Remelting parameters	<i>R1</i>	186	40	Irrelevant	1	55	27.5
	<i>R2</i>	115	10	Irrelevant	1	67	25.3
	<i>R3</i>	162	20	Irrelevant	1	67	25.2
	<i>R4</i>	182	25	Irrelevant	1	67	25.3
	<i>R5</i>	190	25	Irrelevant	1	67	26.4
	<i>R6</i>	200	30	Irrelevant	1	67	25.4
	<i>R7</i>	230	25	Irrelevant	1	78	25.5
	<i>R8</i>	247	25	Irrelevant	1–3	82	25.4

Table 4 –

Material properties used in the calculation of the normalized enthalpy (see Eq. 2).

α_{bulk}	α_{powder}	P [kg/ m^3]	C [J/kg.K]	T_m [K]	L_m [kJ/kg]	D [m^2/s]
0.29 (from [18])	0.5259 (from [18])	7900	490	1640	260000	3.5×10^{-6}

way back. During the process, the chamber is flushed with argon. Additionally, argon is blown over the powder bed from a gas-outlet mounted on the recoater. A more detailed description of the device can be found in [83,84].

A 500 W redPOWER® dual-mode fiber laser (SPI Lasers Ltd, UK) operating at a wavelength of 1070 ± 10 nm is used for melting the material. Both laser (9) and scanning unit (1) are controlled via an SP-ICE-3 board and the WeldMARK software (Raylase GmbH, Germany). The laser beam is collimated as a parallel Gaussian beam into a 2-axis SuperScan III deflection-scanning unit (6) (Raylase GmbH, Germany) with a 15 mm input aperture. Two fused silica mirror galvanometers allow scanning the laser beam over the powder bed. The beam is focused through an F-Theta lens (2) (Sill Optics, Germany) with a 163 mm focal length resulting in a focused beam with a spot size of $13.75 \mu\text{m}$ in radius at $1/e^2$. The laser was utilized in pulsed mode with a pulse frequency of 250 kHz and a nominal laser pulse duration of 2 μs .

Thin walls were printed in keyhole melting mode with the following dimensions: 5 mm length, 250 μm thickness, 750 μm height. As illustrated in Fig. 2, once a wall was fully built, the build plate was moved upwards by 750 μm , and all the powder was removed, to allow *operando* X-ray imaging to be performed through the thickness of the wall during further laser processing. Laser remelting was subsequently done on the top surface of the wall, using a positive defocus to generate large melt pools while favoring the conduction mode.

A CCD camera laser beam profiler (FBP-1KF, CINOGY Technologies, Germany) based on a multi-stage high-performance attenuator with a pixel size of $3.45 \mu\text{m}^2$ was used to measure the laser beam profile at each defocus value. The beam profile was displayed using a beam profiler software (RayCi64 Pro, CINOGY Technologies, Germany). Due to small misalignment of the laser beam through the optical chain, a deviation from Gaussian profile was observed in both defocus directions. Theoretical values of the laser beam spot size at different defocus values were calculated based on Eq. 1, and are reported in Fig. 3a.

$$\omega(z) = \omega_0 \sqrt{1 + \left(\frac{\lambda z}{\pi \omega_0^2} \right)^2} \quad (1)$$

where $\omega_0 = 13.75 \mu\text{m}$ is the beam waist (i.e. smallest radius of the Gaussian beam); z is the scanner position [mm]; $\lambda = 1064$ nm is the laser wavelength.

Different defocus values, resulting in different laser beam sizes and in different intensity profiles, were used for building and remelting the material. Building was performed with a slightly negative defocus ($z = -0.75$ mm) and a high normalized enthalpy (Table 2), ranging between 45 and 60 (using Eq. 2), to favor keyhole pore formation. Remelting was performed at different scanner positions ($z = 1.7$ mm, $z = 2.1$ mm, $z = 2.5$ mm and $z = 2.7$ mm), leading to various positive defocus values, and with a lower normalized enthalpy (Table 3) of about 25, to favor the conduction mode [18]. The corresponding beam shapes, as measured by the camera-based beam profiler, are reported in Fig. 3b.

For LPBF building, three marginally different process parameters (*B1*, *B2*, *B3*) were used, as detailed in Table 2. All remelting parameters (*R1* to *R8*) are listed in Table 3. Due to the significantly larger beam size, remelting was performed using only one line scan. In other words, no hatching was applied during remelting, so that the “hatch distance” parameter is in this case irrelevant. Although in most cases a single remelting pass was used, the effect of applying multiple successive laser passes (up to 3) was evaluated for one set of parameters (*B3-R8*).

The corresponding normalized enthalpies were calculated based on Eq. 2 and are reported in both Tables 2 and 3.

$$\overline{\Delta H} = \frac{\alpha P}{\rho(C\Delta T + L_m)\sqrt{\pi}\omega^3 VD} \quad (2)$$

Where α is the absorptivity of the material, P is the laser power [W], ρ is the density [kg/m^3], C is the specific heat [J/kg.K], ΔT is the difference between the melting temperature and room temperature [K], L_m the latent heat of melting [J/kg], ω the laser spot radius [m], V the laser scanning velocity [m/s], and D the thermal diffusivity [m^2/s]. Material properties used in the present work are reported in Table 4. It should be highlighted that different absorptivity values were used for calculating the normalized enthalpy during building (α_{powder}) and during remelting (α_{bulk}), the absorptivity of the powder α_{powder} being significantly higher than that of the solidified dense metal α_{bulk} [18].

The choice of the remelting process parameters listed in Table 3 was driven by several aspects. A first concern was to maintain a (nearly) constant normalized enthalpy throughout all experiments. This was

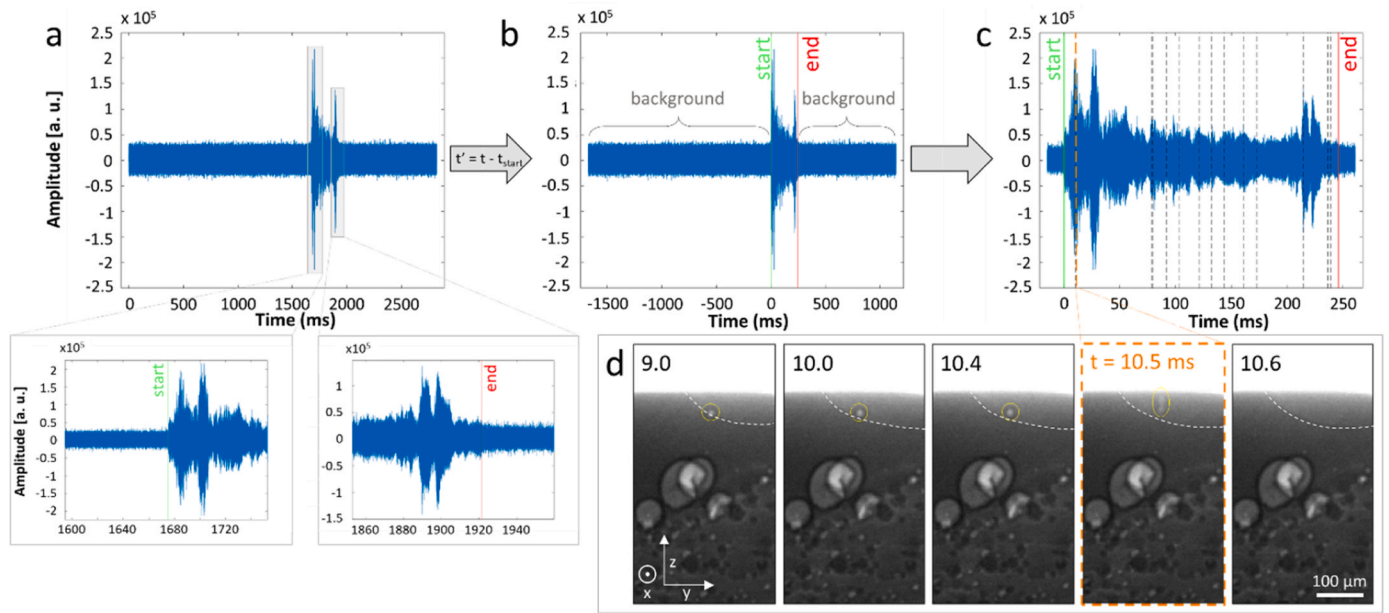


Fig. 4. Overview of the AE signal analysis in the time-domain: a) visualization of the raw signal and identification of the start and end of laser irradiation, b) shifting of the time axis $t' = t - t_{\text{start}}$, c) superposition of the AE signal with the pore removal events identified in the video (discontinuous lines) and d) typical example of a pore removal event, taking place at $t = 10.5$ ms, and highlighted in orange in c). The melt pool boundaries were identified based on differences in grey level and are highlighted by dotted white lines. Building and remelting parameters: B1-R3.

motivated by the fact that the normalized enthalpy can be used to predict the melt pool depth and the threshold for keyhole formation in LPBF [12]. In order to ensure a conduction mode throughout all remelting experiments, the normalized enthalpy was maintained around 25. Several combinations of speed and power resulting in the same normalized enthalpy value were investigated. The second constraint influencing the choice of the process parameters was the relatively low X-ray images acquisition frequency (10 kHz): relatively low scanning speeds (<40 mm/s) were therefore employed. Finally, one of the objectives of the present work was to investigate the effect of the remelting depth on the healing process. To that end, different positive defocus values (resulting in different laser beam radii) were used. The other parameters (power and speed) were adjusted accordingly in order to maintain the normalized enthalpy constant.

2.2. In-situ monitoring conditions

The *operando* X-ray imaging experiments were performed at the TOMographic Microscopy and Coherent rAdiology experimenTs (TOMCAT) beamline of the Swiss Light Source (2.4 GeV machine running at 400 mA) using the previously described LPBF device (Fig. 1). The radiography set-up was located about 28 m from the source (2.9 T bending magnet) and is represented in Fig. 1c. The thin LPBF walls (8) were probed by a parallel X-ray beam (15) with energies ranging between approximately 10 keV and 55 keV. The polychromatic radiation emerging from the source was filtered with 5 mm of Sigradur (50% power filter) and 0.2 mm of Si. The transmitted beam was converted to visible light by a 150 μm thick LuAG:Ce scintillator (Crytur, Czech Republic) located 75 cm after the sample and recorded with a high numerical aperture (NA=0.35) custom-made $4\times$ microscope (14) (Optique Peter, France) [85], coupled to the in-house developed Giga-FRoST detector [86]. This detector exhibits a 2016×2016 pixels commercial CMOS imaging chip with 11 μm pixel size and 12-bit nominal dynamic range, leading to an effective pixel size of 2.75 μm . Its novel readout system provides continuous and sustained data streaming up to almost 8 GB/s (corresponding to a maximum frame rate of 1255 Hz at full frame) to a dedicated high-performance data backend server. The experiments were performed at an acquisition frequency of 10 kHz. This

was achieved by reducing the region of interest to 2016 pixels in width and 200 pixels in height, equivalent to a field-of-view of 5.544×0.55 mm². The image acquisition was automatically triggered by a TTL (Transistor-Transistor Logic) signal provided by the laser control card and serving as a digital synchronization mechanism, with a "low" voltage level close to 0 V and a "high" voltage level between 2 V and 5 V. This approach ensured that the start of the laser was fully synchronized with the start of X-ray acquisition. The number of acquired frames for each series was adjusted according to the laser processing length.

The miniaturized LPBF machine was equipped with a XARION Eta250 Ultra membrane-free optical acoustic sensor, as illustrated in Fig. 1 (10). This microphone was mounted above the build plate, parallel to its top surface, to record airborne noise. This device uses the principle of interferometry to measure sound in a frequency range of 10 Hz to 1 MHz, with a high acquisition rate of 2 MHz. The core of the microphone consists of an optical interferometer made of two semi-transmissive mirrors, arranged at a distance corresponding to a multiple of the laser's half wavelength to induce constructive interference of the transmitted laser beam. Any sound passing the microphone's etalon alters the density of the optical medium, hence changing the local refractive index, which in turn modifies the laser propagation speed and wavelength. As the distance between the two mirrors no longer satisfies the condition for constructive interference, the transmitted laser intensity – measured with a photodiode – changes [87]. The acquisition of the AE signal was started manually, shortly before starting the laser (and thus the X-ray acquisition).

2.3. Image and signal analysis: methodology

The X-ray videos obtained during laser processing were analyzed frame by frame. The last frame at which a given pore was observed before disappearing was identified as the time t of its removal, as illustrated in Fig. 4-d.

Signal analysis was performed using an in-house developed MATLAB code. Thanks to the relatively high signal-to-noise ratio (SNR), a preliminary visualization of the signal in the time-domain allows to clearly distinguish the background noise prior to the start of the laser

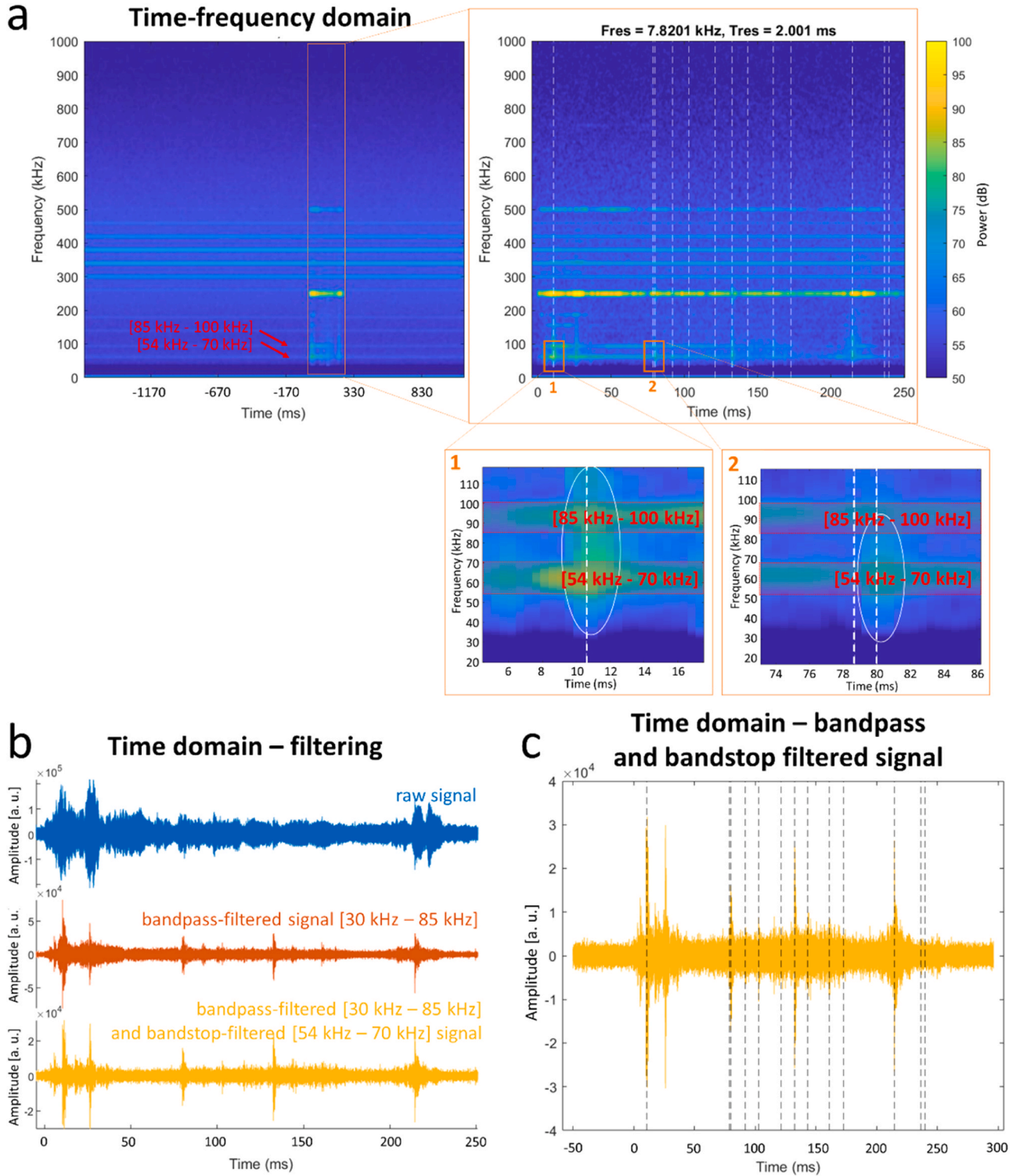


Fig. 5. Overview of the AE signal analysis in the time-frequency domain. a) Spectrogram of the raw signal, with two magnified zones highlighting pore removal events (white dotted lines), the corresponding higher intensity regions (white circles) and the “background noise” frequency bands (in red). b) Effect of band-pass and band-stop filtering on the signal as visualized in the time-domain. c) Resulting filtered signal with superimposed pore-removal events (black dotted lines). Building and remelting parameters: B1-R3.

irradiation, from the signals generated by actual laser processing of a line scan. The start of the laser t_{start} can, therefore, be easily identified as the first major increase in signal intensity, as illustrated in Fig. 4a. A similar approach is adopted to determine the end of the process t_{end} . Based on the value of t_{start} , shifting of the time axis $t' = t - t_{start}$ is performed so that the start of the laser irradiation corresponds to the zero of

the time axis (Fig. 4b). This allows the acoustic signal to be time-aligned with the X-ray videos (Fig. 4c), as the first X-ray image also corresponds to the start of the laser irradiation. Considering that the acoustic signal is acquired with a frequency of 2 MHz, while the X-ray images acquisition rate is of 10 kHz, there is a relatively large tolerance on the identification of t_{start} . For example, an error of 100 points when defining the start

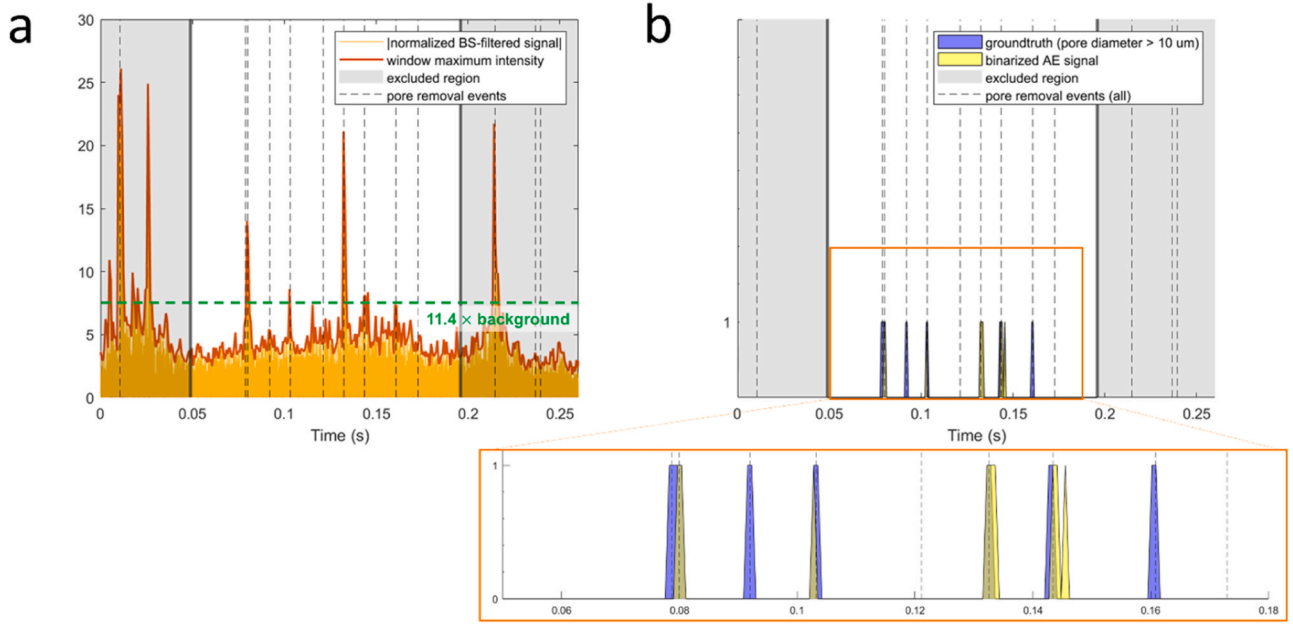


Fig. 6. – a) The bandpass- and bandstop-filtered signal “BS” represented in Fig. 5.c. is normalized using the function $N = \text{normalize}(\text{BS})$ available in Matlab and the absolute value of the normalized signal is computed. In each window of size s , the local maximum signal intensity is determined, and plotted in red. The threshold $i_{th} = 11.4 \times \text{background}$ is marked by a green dotted line. b) Final binarized groundtruth from X-ray images (in blue) and AE signal (in yellow). Building and remelting parameters: B1-R3.

of the process is equivalent to only half of the duration of one X-ray frame, and thus does not significantly impact the time-alignment between the acoustic signal and the X-ray images.

The signal is then analyzed in the time-frequency domain. The spectrogram corresponding to the signal reported in Fig. 4 is drawn in Fig. 5a. It can be observed that pore removal events coincide with high intensity in the [30–100 kHz] frequency range, as stressed by the white circles in Figs. 5a-1 and Figs. 5a-2. At higher frequencies, some high-intensity bands can be observed, particularly at 250 kHz and, to a lower extent, at 500 kHz. These bands are visible from the beginning to the end of laser irradiation, and can be attributed to the 250 kHz pulse frequency of the laser (first and second harmonics). In the frequency range of interest (between 30 kHz and 100 kHz), several lower intensity frequency bands (e.g. [54–72 kHz] and [85–100 kHz]), indicated by the red arrows in Fig. 5a, are present throughout the entire duration of the process. They are visible before the start and after the end of the laser irradiation and intensify during the line scan itself. These bands, which are highlighted in red in Figs. 5a-1 and Figs. 5a-2, correspond to background noise that needs to be filtered out. Based on these observations, a [30–85 kHz] band-pass filter and a [54–72 kHz] band-stop filter are applied on the raw signal, as illustrated in Fig. 5b, to exclude the background noise. The applied filters were minimum-order digital filters, implemented in Matlab with a specified steepness of 0.99 for the transition band. The resulting filtered signal is represented in the time-domain in Fig. 5c, with the superimposed pore-removal events (dotted lines). As illustrated in Fig. 5b, the signal-to-noise ratio is significantly increased after filtering.

The time frame was divided in windows of size s . Based on the X-ray image analysis, a binary “groundtruth” variable was defined as a quantity equal to 1 over a given window size if a pore removal event occurs during this time interval, and equal to 0 otherwise. The window size s was chosen based on the distribution of the time intervals between two successive pore removal events. Various window sizes, ranging from $s = 1040$ points to $s = 6600$ points in the AE signal, were investigated to evaluate the influence of this parameter on the quality of the classification. In 90% of the cases, 2 pore removal events are separated by more than 1040 points, which corresponds to a duration of 0.5 ms, while in

50% of the cases, 2 events are separated by more than 6600 points, corresponding to a duration of 3.3 ms. The resulting spatial resolution ranges between 5 μm and 132 μm , depending on the scanning speed that is being considered.

The size of a pore being one of the factors impacting the final mechanical properties of a part [88], defects below 10 μm were viewed as non-critical. As a result, only the pores with a diameter larger than 10 μm were taken into consideration in the definition of the groundtruth variable. Additionally, to focus on steady-state conditions, the beginning and end of the line scans were not considered in the present study. On both extremities of the wall, a distance of 1 mm was excluded from the analysis. In other words, only the signal corresponding to the central 3 mm of each wall was analyzed.

The bandpass- and bandstop-filtered signal “BS” was normalized using the function $N = \text{normalize}(\text{BS})$ available in Matlab. The absolute value of the normalized AE signal (Fig. 6a) was then binarized using the following approach: in each window of size s , the maximum signal intensity in this window was compared with a threshold value i_{th} . If the maximum signal intensity was higher than i_{th} , the value of the binarized AE signal was set to 1. Otherwise, it was set to 0.

The threshold intensity i_{th} was set to $11.4 \times \text{background}$. For each acquisition, the background was defined as the mean of the absolute value of the normalized AE signal intensity, computed over 10000 acquisition points before the start of the laser (i.e. before $t' = 0$). The value of i_{th} was calculated as follows. For all acquired signals, and for each window, the maximum-intensity-to-background ratio ($\text{peak}/\text{background}$) was computed, considering either windows containing a pore removal event, or windows not containing a pore removal event. The threshold value was defined as the intersection of the two resulting distributions ($(\text{peak}/\text{background})_{\text{pore removal}}$ ratio and $(\text{peak}/\text{background})_{\text{no pore removal}}$ ratio), i.e. 11.4.

The above-described methodology for obtaining a binary groundtruth and a binary AE signal is illustrated in Fig. 6.

Based on all these predictions, the number of true positives TP (i.e. when the groundtruth and binarized AE signal are both equal to 1 in a given window), true negatives TN (groundtruth = 0, binarized AE signal = 0), false positives FP (groundtruth = 0, binarized AE signal = 1) and

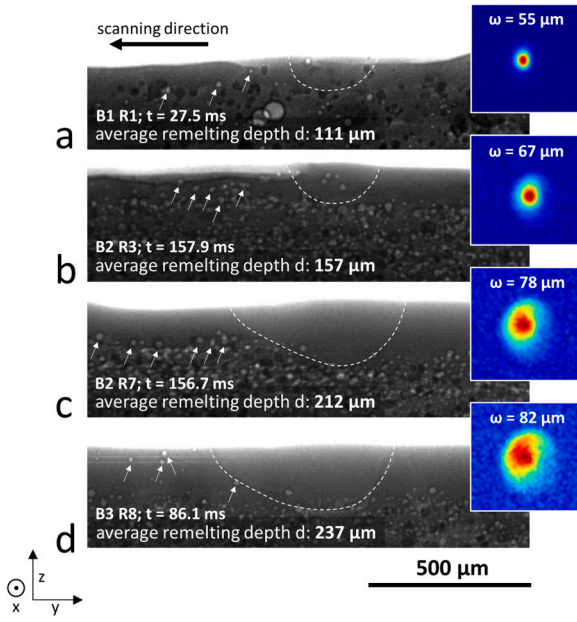


Fig. 7. Radiographs of 4 specimens, processed with various building and remelting parameters reported in Table 2 and Table 3, respectively. Each snapshot is taken at a time t after the start of laser remelting. The corresponding laser spot profiles are also shown. The melt pool boundaries are highlighted by dotted white lines. Increasing the defocus towards larger positive values from (a) to (d), while maintaining the normalized enthalpy constant, leads to an increase in melt pool depth and, thus, in a deeper pore-free region after remelting. The corresponding videos can be found in the “Supplementary” section.

false negatives FN (groundtruth = 1, binarized AE signal = 0) were determined, from which the *accuracy* (Eq. 3), *precision* (Eq. 4), *recall* (Eqs. 5) and *F1-score* (Eq. 6) could be derived.

$$accuracy = \frac{TP + TN}{FP + TP + FN + TN} \quad (3)$$

$$precision = \frac{TP}{FP + TP} \quad (4)$$

$$recall = \frac{TP}{TP + FN} \quad (5)$$

$$F1 - score = \frac{2 \cdot precision \cdot recall}{precision + recall} \quad (6)$$

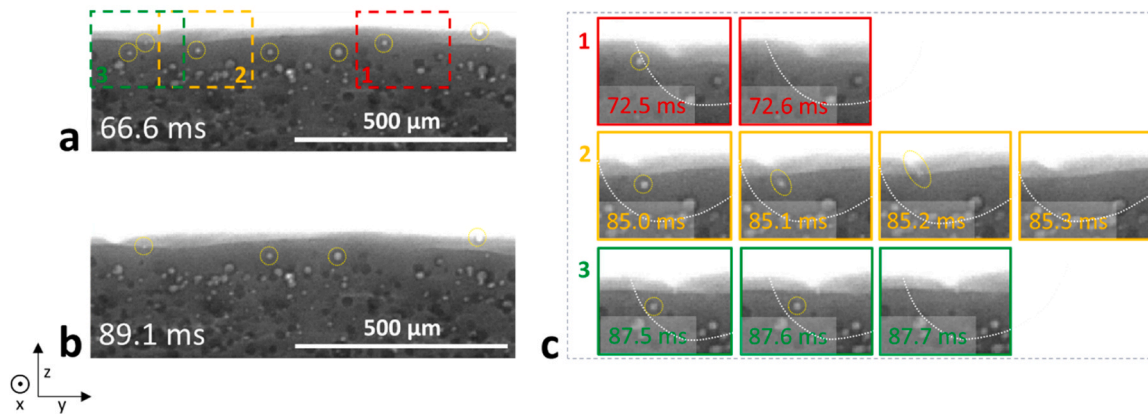


Fig. 8. Radiographs of a specimen built and remelted with parameters B1-R1, (a) before and (b) after remelting. (c) Frame-by-frame focus on 3 different regions during laser remelting. The pores highlighted in regions 1 and 3 disappear at a distance from the surface, while the pore located in region 2 moves upwards and disappears as it reaches the top surface. The melt pool boundaries are highlighted by a dotted white line.

3. Results and discussion

3.1. Operando observation of defects healing

3.1.1. Effect of defocusing on healing depth

Fig. 7 and the corresponding Videos 1–4 (see supplementary videos) report four illustrative examples of remelting line scans, performed with various process parameters (see Table 2 and Table 3 for the detailed melting and remelting laser parameters). It can be noticed that although a number of pores (highlighted by white arrows in Fig. 7) are present before the laser pass (i.e. on the left side of the melt pool in Fig. 7), the amount of pores in the top region of the wall decreases after remelting (i.e. on the right side of the melt pool). This is particularly visible in Videos 2–4. Similar observations can be made from Fig. 8 and Fig. 9: when comparing the top region of the wall before (a) and after (b) remelting, the number of pores is significantly reduced. Overall, these figures indicate that the present strategy can successfully reduce porosity content in the sub-surface region of the wall. As illustrated in Fig. 7, remelting was performed with different positive defocus values to evaluate the effect of an increase in beam size on the efficiency of porosity removal. Based on Eq. 2, laser power and speed were adjusted such as to maintain the normalized enthalpy approximately constant ($25.2 < \overline{\Delta H} < 27.5$). Increasing the defocus towards larger positive values leads to an increase in the melt pool depth, from 111 μm to 237 μm for a beam radius ω of 55 μm and 82 μm , respectively. The depth at which porosity healing occurs increases accordingly, as can be observed in Fig. 7 and in Videos 1–4: the pore-free region on the right side of the melt pool extends deeper in Fig. 7d (Video 4) than in Fig. 7a (Video 1). In other words, depending on how deep the defects lie, the process parameters can be finely adjusted to reach a sufficient depth and to remove the pores lying at such depth. However, healing deeper defects requires larger laser spot sizes, resulting in larger melt pools, which may reduce the overall dimensional accuracy. This should not be an issue in the bulk regions of LPBF parts [89] but could be more detrimental when sharp edges and fine features are considered.

Supplementary material related to this article can be found online at [doi:10.1016/j.addma.2023.103880](https://doi.org/10.1016/j.addma.2023.103880).

A more detailed, frame-by-frame analysis of the pore trajectories upon interaction with the melt pool allows identifying different types of healing behavior, as evidenced in Fig. 8. In the area documented by Fig. 8a, three pores are removed upon laser remelting and are no longer visible afterwards (Fig. 8b). These pores are located in the regions identified as “1”, “2”, and “3”, which are magnified and analyzed frame by frame in Fig. 8c.

The first type of trajectory is exemplified by the pore located in

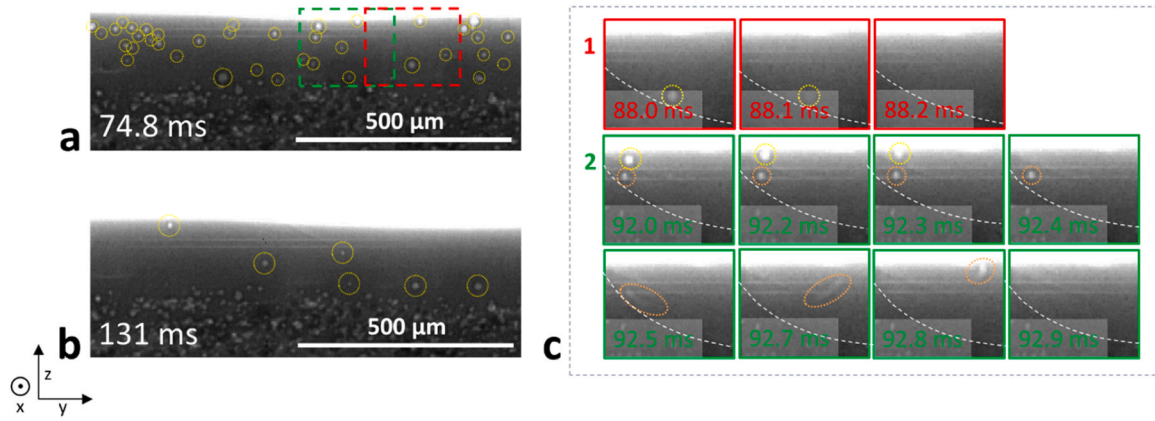


Fig. 9. Radiographs of a specimen built and remelted with parameters B3-R8, (a) before and (b) after remelting. (c) Frame-by-frame focus on 2 different regions during laser remelting. The pore located in region 1 disappears at a distance from the surface, while the two pores located in region 2 move upwards and disappear as they reach the top surface. The melt pool boundaries are highlighted by a dotted white line.

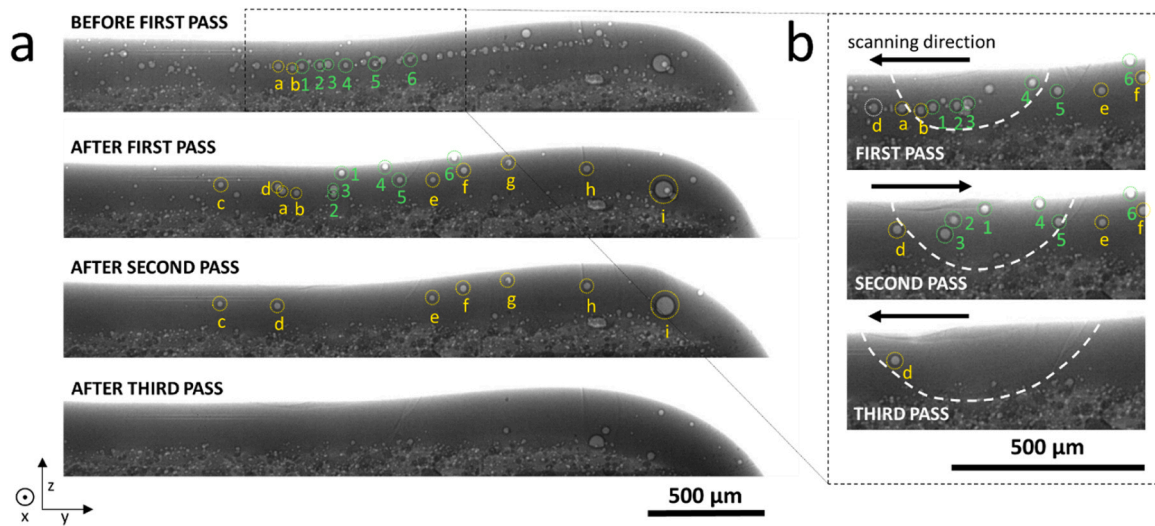


Fig. 10. Effect of multiple successive laser passes. The building and remelting parameters are B3-R8. (a) Snapshots of the right side of the wall before and after each laser pass. (b) Snapshots taken in the position highlighted in (a) during three successive laser remelting passes. The melt pool boundaries are highlighted by a dotted white line.

region “2”. As it encounters the melt pool, the pore moves upwards and disappears when it reaches the top surface. In the two other cases, i.e. regions “1” and “3”, an upward movement of the pore is not visible and the pore seems to disappear at a distance from the top surface. In this case, it is believed that the pore either travels too fast compared to the imaging frame rate, or moves horizontally (i.e. along the x direction, to the back or to the front of the wall) until it reaches a side surface, so that its motion is invisible in the 2D radiographs, only providing a projection of the wall volume.

Fig. 9 provides another typical example of these distinctive healing behaviors: no vertical motion is observed prior to the disappearance of the pore located in region “1”, while the two pores located in region “2” move upwards and disappear after reaching the top surface.

In addition to the above-described healing behaviors, some pores, although they significantly interact with the melt pool, do not escape to the top or side surfaces, and remain trapped as the metal solidifies. This is illustrated in Fig. 10 and will be more extensively described in the next section.

3.1.2. Effect of multiple passes on porosity removal

As shown in Fig. 8 and Fig. 9, in the presence of multiple pores in the top region of the part, a single remelting pass is often insufficient to

remove all of them. Fig. 10 illustrates that, although most pores are removed after the first remelting pass, a number of defects remain present, which are eventually healed upon a second or third pass. This multi-step healing can be attributed to a combination of two factors.

A first factor lies in the fact that a pore has a statistically higher chance to escape if its interaction time with the melt pool is increased [32]. Applying a higher number of remelting cycles can increase the total duration during which a given pore interacts with the melt pool and, thus, favor its removal. This type of behavior is illustrated by pores 1–6, highlighted in green in Fig. 10. These pores were displaced to some extent by the first laser pass – particularly pores 1, 4 and 6 which moved closer to the top surface – but got trapped at some point by the moving solidification front, thus preventing them from reaching the surface and disappear. Increasing the interaction time via a second melt pool pass then allowed to successfully remove them.

A second aspect is related to the fact that, upon each additional remelting pass, the melt pool dimensions increase progressively, due to the heat accumulated in successive scans. This phenomenon can be clearly visualized in Fig. 10b, in which the melt pool length and depth respectively increase from 402 μm to 623 μm and from 150 μm to 194 μm between the first and third pass. This also translates into an increase in the width of the melt pool, i.e. along the x direction, which

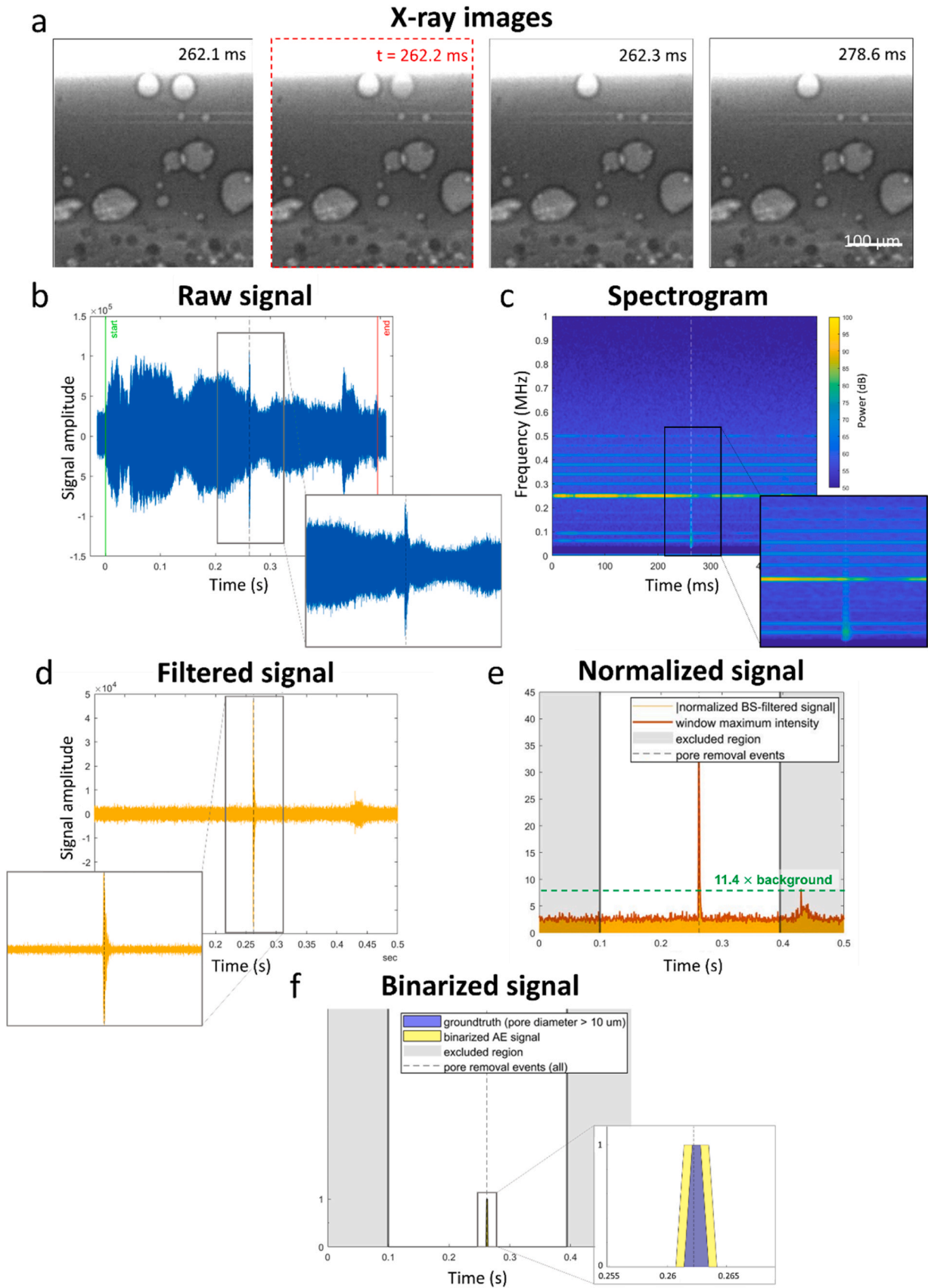


Fig. 11. Line scan B1-R2: (a) X-ray images before, during and after a single pore removal event occurring at $t = 262.2$ ms. Raw AE signal in the time-domain (b) and in the time-frequency domain (c), filtered signal in the time-domain (d), absolute value of the normalized signal (e), binarized groundtruth and binarized AE signal (f) (window size of 2180 points). The pore removal event at $t = 262.2$ ms in (b), (c), (d), (e) and (f) is highlighted by a dotted line. The threshold $i_{th} = 11.4 \times \text{background}$ is marked by a green dotted line in (e).

Table 5

Accuracy, precision, recall and F1-score obtained for the B1-R2 line scan, using a window size s of 2180 points.

Accuracy	Precision	Recall	F1-score
0.99	0.5	1	0.67

Table 6

Accuracy, precision, recall and F1-score obtained for each line scan, using a window size of 2180 points.

Line scan	Number of events ($O > 10 \mu\text{m}$)	Accuracy	Precision	Recall	F1-score
B1-R2	1	0.99	0.50	1.00	0.67
B1-R3	7	0.94	0.86	0.46	0.60
B1-R7	11	0.70	0.37	0.82	0.51
B2-R4	11	0.73	0.28	0.35	0.31
B2-R5	14	0.79	0.47	0.67	0.55
B3-R8	49	0.64	0.64	0.96	0.77
Weighted average	Total number of events: 94	0.71	0.56	0.79	0.64

cannot be visualized on the radiographs. Hence, pores that are located further away from the center of the line scan might not interact with the melt pool in the first pass but be subsequently removed as the melt pool becomes wider along the x direction. This is the case of pores a and b , which are highlighted in yellow in Fig. 10. They remain stationary during the first pass but are successfully removed as the laser comes back for a second pass. Similarly, pore c does not interact with the melt pool during the first and second pass, but disappears during the third remelting cycle.

The use of multiple remelting passes can thus greatly increase the healing efficiency, through the combined effect of extended interaction time between pore and melt pool, and increased melt pool dimensions. However, as previously mentioned for large positive defocus values (Section 3.1.1), a melt pool broadening might have a detrimental impact on the dimensional accuracy of the final parts. To circumvent this drawback, while maximizing the chances for pores to escape, a time delay between two successive remelting passes can be implemented, so that heat accumulation does not occur and the melt pool size remains constant [90]. Alternatively, for larger structures, applying several adjacent remelting line scans separated by a reduced hatch distance, can increase the healing efficiency as well, while limiting the broadening of the melt pool. This aspect was not investigated in the present study due to the small thickness of the wall, as required to perform X-ray imaging successfully. It should also be highlighted that only one combination of process parameters (B3-R8) was used in the present study to evaluate the effect of multiple remelting passes on the healing efficiency. Future work should not only validate this approach on bulkier parts, but also evaluate its applicability when using other process parameters.

In conclusion, laser beam defocusing and number of remelting passes complement each other towards optimizing healing efficiency, as they allow the melt pool dimensions and the pore/melt pool interaction time to be finely tuned. However, they should be used with caution to maintain a good dimensional accuracy.

Laser remelting has been reported to favor a so-called “edge effect”, i.e. to affect the flatness of the top surface by the formation of edges due to remelted metal being pushed by the laser beam [35]. On the other hand, multiple authors have documented a positive effect of laser remelting in terms of surface roughness reduction [32–35,91], and reported that the improvement in top surface quality increases with the number of remelting cycles [32,91]. Remelting is indeed known to smoothen the surface by removing residual adherent powder particles and spatters. Although beyond the scope of the present paper, the effect of remelting with a positively defocused beam on the final geometry and overall surface quality should be investigated on larger parts, as conclusions on these matters cannot be drawn from a thin wall geometry.

3.2. Signal analysis

3.2.1. Case 1: line scan B1-R2.

Using the methodology detailed in Section 2.3, the acoustic signal acquired during remelting and the corresponding time-aligned X-ray images were analyzed, for a total of 6 single line scans processed with various remelting parameters (R2, R3, R4, R5, R7, R8), as detailed in Table 3.

Among these 6 line scans, the analysis of one of them is extensively detailed in the present section, as an illustrative example. The results of the analysis of the other line scans are summarized in the following sections.

In line scan B1-R2, one single pore is removed during the entire laser remelting pass. This unique pore removal event, illustrated in Fig. 11a, takes place 262.2 ms after the start ($t = 0$) of the laser. This time is highlighted as a black dotted line on the raw acoustic signal in the time-domain (Fig. 11b) and appears to coincide with a distinctive peak in signal intensity. Similar observations can be made when analyzing the raw signal in the time-frequency domain (Fig. 11c), and the filtered signal in the time-domain (Fig. 11d). In the spectrogram reported in Fig. 11c, the intensity is locally higher over a [20–350 kHz] frequency range, with the maximum intensities being observed between 30 kHz and 100 kHz. After applying a [30–85 kHz] band-pass filter and a [54–72 kHz] band-stop filter, the signal intensity at $t = 262.2$ ms is more than 10 times higher than the rest of the signal (Fig. 11d). Fig. 11f demonstrates a good overlap between the binarized acoustic signal and the binarized groundtruth, which results in a high accuracy and recall of respectively 0.99 and 1, a precision of 0.5 and an F1-score of 0.67, as reported in Table 5. We should highlight that this overlap and the resulting accuracy, precision, recall and F1-score directly depend on the window size s , as will be illustrated and discussed in Section 3.2.3.

The accuracy is defined as the proportion of correct predictions (both true positives and true negatives) among the total number of cases examined (i.e. true positives, true negatives, false positives and false negatives). A high accuracy does not necessarily mean that most of the pore removal events have been successfully detected. If only one or a few pore removal events are present (as is the case in this example with a single pore removal), the accuracy might still be high even if these events are not detected, as long as most of the “non-events” are correctly identified as such.

The recall quantifies how many relevant items are retrieved. In other words, a low recall would mean that many pore removal events are not detected even though they actually took place. In the present case, a recall value of 1 indicates that the unique pore removal event was successfully identified as such by means of AE monitoring.

The precision quantifies how many retrieved items are relevant. In other words, a low precision would mean that healing is detected even though it did not occur. This could be the case, for example, if events other than healing but with a similar AE footprint happen at a given time, resulting in false positives in the prediction. In the present case, for a window size $s = 2180$ points (which corresponds to a duration of 1.09 ms), when analyzing the X-ray images frame by frame, the pore removal event is identified at $t = 262.2$ ms. The groundtruth is 1 in the two time windows directly surrounding this pore removal event, namely in $t = 261.98$ ms and in $t = 263.07$ ms. However, due to the fact that the maximum AE signal intensity is higher than i_{th} over a longer time interval than the binarized groundtruth, the binarized AE signal is found to be equal to 1 in four time windows, namely in $t = 260.89$ ms, $t = 261.98$ ms, $t = 263.07$ ms, and $t = 264.16$ ms. As a result, a relatively low precision of $2/4 = 0.5$ is obtained. However, as will be discussed below (Section 3.2.3), the precision can be improved by increasing the window size s .

For monitoring, a high precision is essential, to ensure that if healing is detected, it did really occur. A low precision would induce bad monitoring-based decision making (i.e. considering that the pore has been healed when it is in fact still present in the material, with a

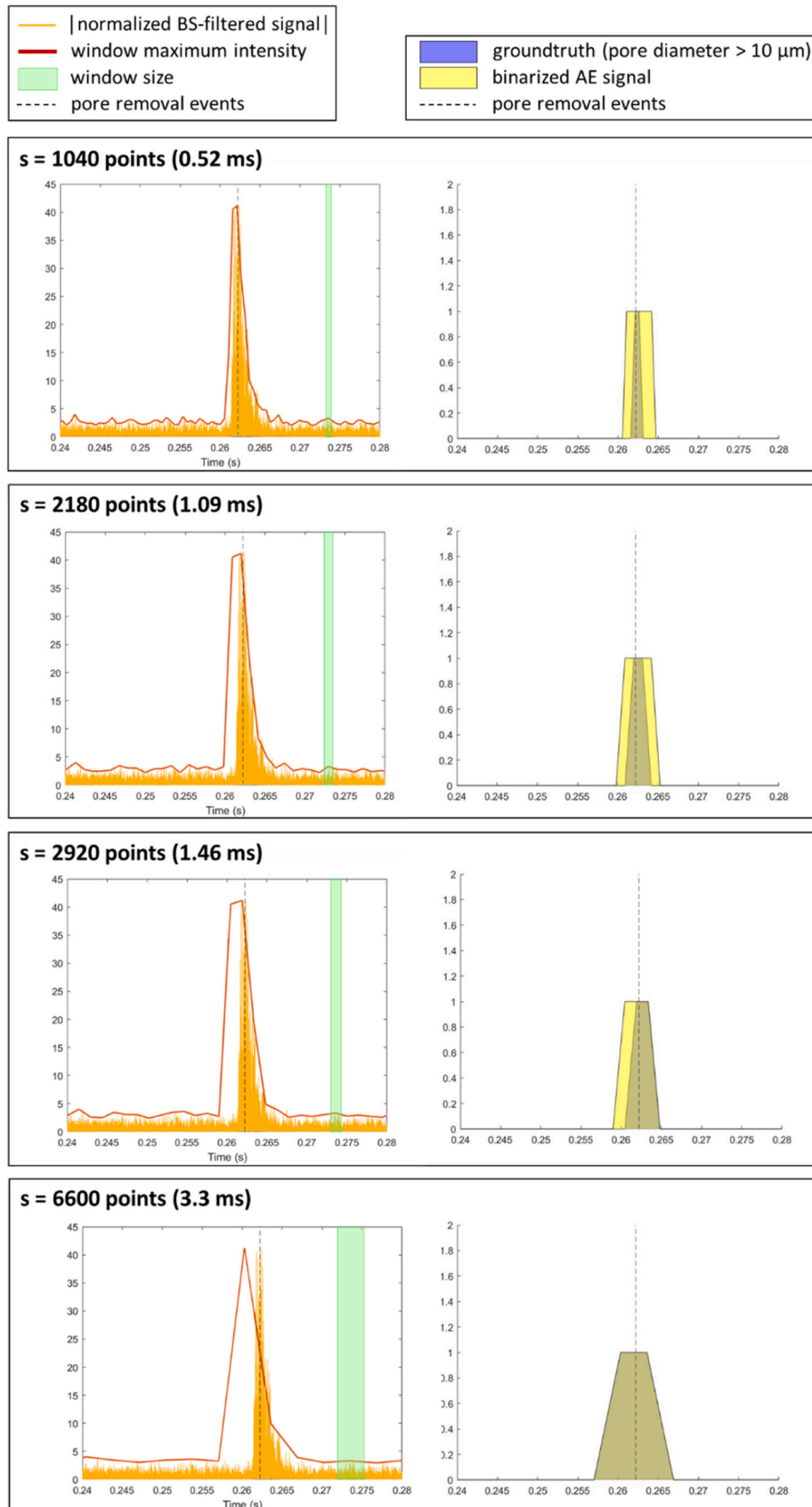


Fig. 12. Line scan B1-R2: Effect of the window size ($s = 1040$ points, 2180 points, 2920 points and 6600 points) on the overlap between the binarized AE signal and the groundtruth. The pore removal event at $t = 262.2$ ms is highlighted by a black dotted line. The window size is highlighted in green.

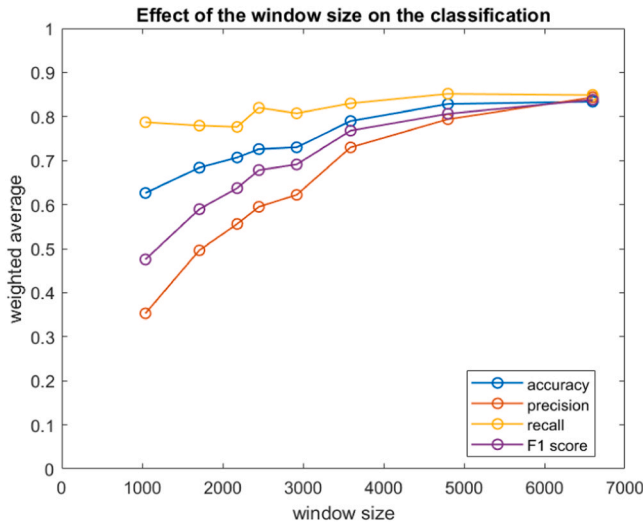


Fig. 13. Effect of window size on classification accuracy, precision, recall and F1-score.

potentially detrimental effect on the final properties of the part). On the other hand, a high *recall* is also critical. If the *recall* score is too weak (for example, if the ratio between the AE signature of a pore removal event and the background noise is too low), it would imply that a significant fraction of the pore removal events that actually occurred were not detected, making the monitoring technique ineffective. As the harmonic mean of *precision* and *recall*, the *F1-score* provides a good indication of the overall quality of the classification.

Taking the above-discussed aspects into consideration, the analysis of 5 other representative cases is detailed in Section 3.2.2.

3.2.2. Overview of other cases

The same methodology was applied to the five other line scans. Considering a relatively small window size of 2180 points, the resulting *accuracy*, *precision*, *recall* and *F1-score* are reported in Table 6. In total, 94 pore removal events were identified in the X-ray image analysis of the six single line scans.

3.2.3. Effect of window size

Increasing the window size can help reaching a better overlap between the binarized AE signal and the groundtruth, by enlarging the time interval over which the binarized AE signal is equal to 1. This is illustrated for line scan B1-R2 in Fig. 12: as the window size increases from $s = 1040$ points to $s = 6600$ points, the overlap between the groundtruth (in blue) and the binarized AE signal (in yellow) increases accordingly, to reach 100% for $s = 6600$ points. In other words, for this window size, the *accuracy*, *precision*, *recall* and *F1-score* for line scan B1-R2 are equal to 1.

Fig. 13 provides an overview of the effect of the window size on these

4 parameters. The average *accuracy*, *precision*, *recall* and *F1-score* values, weighted by the number of events identified in a given line scan (based on the analysis of the corresponding X-ray images), are reported as a function of the window size, for a total of eight different window size values.

As can be observed in Fig. 13, the *accuracy*, *precision*, *recall* and *F1-score* increase as the window size increases. This can be explained by a combination of two factors. First, the smaller the window size, the lower the overlap between the binarized groundtruth and the binarized AE signal, as illustrated and discussed for line scan B1-R2 (Fig. 12). Second, some pore removal events might have a low or non-detectable acoustic signature. Increasing the window size increases the probability for two or more pore removal events to occur in the same window and, thus, the probability for at least one of these events to have a detectable acoustic signature.

When computing the distribution of the time intervals separating the 94 pore removal events identified in all 6 experiments, 10% of these time intervals are shorter than 0.52 ms (i.e. a window size of 1040 points), while 50% are shorter than 3.3 ms (window size of 6600 points). These results are summarized in Table 7.

Therefore, for a window size s of 1040 points, the probability to have two or more healing events in the same window is 10%, while for $s = 6600$ points, this probability reaches 50% (based on the statistics obtained over all pore removal events identified in the present study).

In other words, in the current configuration, the exact number of pores removed whenever healing is detected in a given window cannot be established with certainty, particularly for larger window sizes. This is a noteworthy drawback to the observed improvement in *accuracy*, *precision*, *recall* and *F1-score* when the window size increases.

The change in window size also influences the temporal and spatial resolution of the prediction. The time resolution achieved in the present work is in the same range as that reported in other works using AI for real-time detection of process instabilities (as an example, Shevchik et al. [43] achieved temporal resolutions down to 2 ms). As for the spatial resolution, depending on the scanning speed (Table 7), a window size of 1040 points corresponds to a distance of 5.2–20.8 μm . This distance reaches a value of 33–132 μm when considering a window size of 6600 points. By comparison, the smallest diameter of the defocused laser beam used to perform remelting in the present study was 110 μm . In other words, even for a relatively large window size, the spatial resolution remains high, when compared to the beam size.

The results obtained for $s = 6600$ points illustrate that the occurrence of healing can be monitored with a relatively high *accuracy*, *precision*, *recall* and *F1-score* and with a very high spatial resolution. While *accuracy*, *precision*, *recall* and *F1-score* are expected to increase significantly if artificial intelligence tools (Machine Learning algorithms) are used to identify the exact AE signatures of healing, the associated spatial resolution remains to be evaluated.

Based on the straightforward signal analysis methodology presented in this work, the *precision* lies around 80% for a window size $s = 6600$ points. This means that if a pore removal event is detected, there is a

Table 7

Window sizes and their corresponding duration, distance (dependent on the laser remelting speed) and probability to have two or more events occurring in the same window.

Window size [number of points]	1040	1710	2180	2450	2920	3590	4800	6600
Duration [ms]	0.52	0.855	1.09	1.225	1.46	1.795	2.4	3.3
Distance [μm]								
R2 (10 mm/s)	5.2	8.55	10.9	12.25	14.6	17.95	24.0	33.0
R3 (20 mm/s)	10.4	17.1	21.8	24.5	29.2	35.9	48.0	66.0
R4, R5, R7, R8 (25 mm/s)	13.0	21.38	27.25	30.63	36.5	44.88	60.0	82.5
R6 (30 mm/s)	15.6	25.65	32.7	36.75	43.8	53.85	72.0	99.0
R1 (40 mm/s)	20.8	34.2	43.6	49	58.4	71.8	96	132
% of time intervals between two adjacent events lower or equal to this duration	10	15	20	25	30	35	40	50

20% probability that healing actually did not occur. Besides, considering that the *recall* lies around 80% for a window size $s = 6600$ points, about 20% of the time windows containing at least one pore removal event are not identified as such by the monitoring system. In view of this non negligible uncertainty in the prediction, it is recommended to perform multiple remelting iterations of any given defective layer to maximize the chances for healing to successfully take place. Based on previous observations (Section 3.1.2), a good practice in terms of balance between defect minimization and productivity optimization would be to do 3 successive remelting passes, whenever porosity is detected in the material during LPBF.

4. Conclusions

In order to remove deep keyhole-type defects during LPBF processing, a new approach has been implemented and tested in a miniaturized-LPBF device specifically designed for *operando* synchrotron X-ray measurements. The healing strategy consists in remelting the top surface with a positively defocused laser beam, while maintaining a relatively low normalized enthalpy value. This allows obtaining a conduction mode melting regime, yet sufficiently deep to reach keyhole pores generated by previous laser passes.

X-ray imaging allows visualizing the interaction of keyhole pores with the melt pool during laser remelting. The pores tend to move upwards or sideways, resulting in their elimination as they reach the top or side surface. However, a number of pores may not be healed by a single laser pass, either because they do not interact with the melt pool, or because they are trapped by the moving solidification front.

The influence of two key remelting parameters is investigated: the extent to which the beam is defocused, and the number of successive remelting passes. Both factors tend to improve healing efficiency, either by increasing the melt pool dimensions (and, thus, the probability for a pore to interact with the melt pool) or by extending the pore/melt pool interaction time (and, thus, the probability for a pore to escape to an external surface). However, these processing parameters should be used with caution and finely tuned to maintain a good dimensional accuracy of the part. The effect of remelting with a positively defocused beam on the final geometry and surface quality remains a topic to investigate, as well as its influence on the microstructure of the material and its mechanical properties.

One side-effect of a remelting operation meant for defect removal during LPBF processing is the overall increase in build time that it induces. Laser remelting can only be beneficial if the achieved quality enhancement outweighs the time cost. Hence, it is essential to associate it with in-situ monitoring. Only in the event that an unstable keyhole regime is detected (e.g. by means of AE monitoring [31,57,60]), should remelting be applied on the defective layer. In that case it is worth performing healing, even with a low speed and with multiple remelting passes, as this might help circumvent time-consuming post-process treatments such as HIP.

The same AE monitoring set-up can then be used for (i) detecting unstable keyhole regime during building, as already demonstrated by Hamidi et al. [31], and (ii) measuring whether or not healing has been successfully achieved upon remelting, as illustrated in the present paper. Combining monitoring of defect formation and defect removal is an essential step towards elimination of expensive post-process quality control of the part. In the direct continuation of the work of Hamidi et al. [31], the present paper demonstrates for the first time that a highly sensitive airborne acoustic microphone can be used to monitor the healing of keyhole pores. Through a simple signal analysis methodology, it is shown that the removal of a pore can have a clear acoustic signature. Pore removal events are identified with a relatively high *accuracy*, *precision*, *recall* and *F1-score*, and with a high spatial resolution ($< 150 \mu\text{m}$ for the process parameters considered in this study).

The present exploratory work paves the way towards more in-depth signal analysis and the use of AI tools to refine the AE signature of

healing and mitigate possible sources of error or uncertainty. However, this will require an extensive signal database for porosity healing and, thus, the acquisition of a high number of AE measurements, which goes beyond the scope of the present paper.

In order to validate the applicability of the proposed method on a larger scale, similar experiments should be reiterated on bulkier parts, in a conventional LPBF device equipped with acoustic emission monitoring. The efficiency of healing, as well as the effect of laser beam remelting on the microstructure and mechanical properties of the material, could be assessed by comparing “healed” parts with “as-built” ones, using post-process destructive or non-destructive analysis techniques. This validation work remains a key step to determine to what extent the present approach can impact the final performance of laser-remelted LPBF parts.

Finally, future work could also evaluate the effect of a similar strategy on different materials, or on the removal of other types of defects, such as cracks, and the corresponding monitoring by AE.

CRedit authorship contribution statement

Lucas Schlenger: Writing – review & editing, Investigation, Data curation. **Petegem Steven Van:** Writing – review & editing, Resources, Investigation, Funding acquisition. **Giulio Masinelli:** Writing – review & editing, Software, Formal analysis. **Roland E. Logé:** Writing – review & editing, Supervision, Project administration, Funding acquisition. **Charlotte de Formanoir:** Writing – original draft, Visualization, Software, Project administration, Methodology, Investigation, Formal analysis, Data curation, Conceptualization. **Nasab Milad Hamidi:** Writing – review & editing, Software, Project administration, Methodology, Investigation, Formal analysis. **Federica Marone:** Writing – review & editing, Resources, Data curation. **Antti Salminen:** Writing – review & editing, Resources. **Ashish Ganvir:** Writing – review & editing, Resources. **Kilian Wasmer:** Writing – review & editing, Resources, Funding acquisition.

Declaration of Competing Interest

The authors declare that they have no known competing financial interests or personal relationships that could have appeared to influence the work reported in this paper.

Data Availability

Data will be made available on request.

Acknowledgements

We acknowledge the Paul Scherrer Institut (PSI), Villigen, Switzerland, for the provision of synchrotron radiation beamtime at the TOMCAT beamline X02DA of the SLS. We thank the Swiss National Science Foundation (SNSF) for the funding of the project "CRSII5_193799 / 1" entitled "In-situ monitoring in additive manufacturing of metals and alloys based on artificial intelligence". LS and REL acknowledge funding from the SMARTAM project, within the Strategic Focus Area Advanced Manufacturing (SFA-AM) initiative of the ETH Board in Switzerland. University of Turku thanks Business Finland and Academy of Finland for the financial support received through DREAMS and GREEN-BAT project, respectively. In addition, Prof. Ganvir also thanks University of Turku for financial support through internal tenure-track grant. Our gratitude goes to Mathijs van der Meer for his precious technical expertise, to Dr. Vigneashwara Pandiyan and Dr. Sneha Goehl for their assistance during the setup of the XARION sensor at the TOMCAT beamtime, as well as to Reza Esmaeilzadeh, Claire Navarre and Tri Le Quang for their support during synchrotron measurements. All members of the Thermomechanical Metallurgy Laboratory at EPFL acknowledge the generous financial

support of PX Group to the laboratory.

References

- [1] W.E. King, A.T. Anderson, R.M. Ferencz, N.E. Hodge, C. Kamath, S.A. Khairallah, A. M. Rubenchik, Laser powder bed fusion additive manufacturing of metals; physics, computational, and materials challenges, *Appl. Phys. Rev.* 2 (2015), 041304, <https://doi.org/10.1063/1.4937809>.
- [2] T. DebRoy, H.L. Wei, J.S. Zuback, T. Mukherjee, J.W. Elmer, J.O. Milewski, A. M. Beese, A. Wilson-Heid, A. De, W. Zhang, Additive manufacturing of metallic components – process, structure and properties, *Prog. Mater. Sci.* 92 (2018) 112–224, <https://doi.org/10.1016/j.pmatsci.2017.10.001>.
- [3] S. Tammam-Williams, P.J. Withers, I. Todd, P.B. Prangnell, The influence of porosity on fatigue crack initiation in additively manufactured titanium components, *Sci. Rep.* 7 (2017), 7308, <https://doi.org/10.1038/s41598-017-06504-5>.
- [4] E.W. Jost, J.C. Miers, A. Robbins, D.G. Moore, C. Saldana, Effects of spatial energy distribution-induced porosity on mechanical properties of laser powder bed fusion 316L stainless steel, *Addit. Manuf.* 39 (2021), 101875, <https://doi.org/10.1016/j.addma.2021.101875>.
- [5] M. Hamidi Nasab, S. Romano, D. Gastaldi, S. Beretta, M. Vedani, Combined effect of surface anomalies and volumetric defects on fatigue assessment of AlSi7Mg fabricated via laser powder bed fusion, *Addit. Manuf.* 34 (2020), <https://doi.org/10.1016/j.addma.2019.100918>.
- [6] J.V. Gordon, S.P. Narra, R.W. Cunningham, H. Liu, H. Chen, R.M. Suter, J.L. Beuth, A.D. Rollett, Defect structure process maps for laser powder bed fusion additive manufacturing, *Addit. Manuf.* 36 (2020), 101552, <https://doi.org/10.1016/j.addma.2020.101552>.
- [7] S.M.H. Hojjatzadeh, N.D. Parab, Q. Guo, M. Qu, L. Xiong, C. Zhao, L.I. Escano, K. Fezzaa, W. Everhart, T. Sun, L. Chen, Direct observation of pore formation mechanisms during LPBF additive manufacturing process and high energy density laser welding, *Int. J. Mach. Tools Manuf.* 153 (2020), 103555, <https://doi.org/10.1016/j.jmachtools.2020.103555>.
- [8] R. Cunningham, A. Nicolas, J. Madsen, E. Fodran, E. Anagnostou, M.D. Sangid, A. D. Rollett, Analyzing the effects of powder and post-processing on porosity and properties of electron beam melted Ti-6Al-4V, *Mater. Res. Lett.* 5 (2017) 516–525, <https://doi.org/10.1080/21663831.2017.1340911>.
- [9] A. Bobel, L.G. Hector, I. Chelladurai, A.K. Sachdev, T. Brown, W.A. Poling, R. Kubic, B. Gould, C. Zhao, N. Parab, A. Greco, T. Sun, In situ synchrotron X-ray imaging of 4140 steel laser powder bed fusion, *Materialia* 6 (2019), 100306, <https://doi.org/10.1016/j.mta.2019.100306>.
- [10] A. Mostafaei, C. Zhao, Y. He, S. Reza Ghiaasiaan, B. Shi, S. Shao, N. Shamsaei, Z. Wu, N. Kouraytem, T. Sun, J. Pauza, J.V. Gordon, B. Webler, N.D. Parab, M. Asherloo, Q. Guo, L. Chen, A.D. Rollett, Defects and anomalies in powder bed fusion metal additive manufacturing, *Curr. Opin. Solid State Mater. Sci.* 26 (2022), 100974, <https://doi.org/10.1016/j.cossms.2021.100974>.
- [11] H. Gong, K. Rafi, H. Gu, T. Starr, B. Stucker, Analysis of defect generation in Ti-6Al-4V parts made using powder bed fusion additive manufacturing processes, *Addit. Manuf.* 1 (2014) 87–98, <https://doi.org/10.1016/j.addma.2014.08.002>.
- [12] W.E. King, H.D. Barth, V.M. Castillo, G.F. Gallegos, J.W. Gibbs, D.E. Hahn, C. Kamath, A.M. Rubenchik, Observation of keyhole-mode laser melting in laser powder-bed fusion additive manufacturing, *J. Mater. Process. Technol.* 214 (2014) 2915–2925, <https://doi.org/10.1016/j.jmatprotec.2014.06.005>.
- [13] M.Hamidi Nasab, D. Gastaldi, N.F. Lecis, M. Vedani, On morphological surface features of the parts printed by selective laser melting (SLM), *Addit. Manuf.* 24 (2018) 373–377, <https://doi.org/10.1016/j.addma.2018.10.011>.
- [14] A. du Plessis, Effects of process parameters on porosity in laser powder bed fusion revealed by X-ray tomography, *Addit. Manuf.* 30 (2019), 100871, <https://doi.org/10.1016/j.addma.2019.100871>.
- [15] S. Romano, A. Abel, J. Gumpinger, A.D. Brandão, S. Beretta, Quality control of AlSi10Mg produced by SLM: metallography versus CT scans for critical defect size assessment, *Addit. Manuf.* 28 (2019) 394–405, <https://doi.org/10.1016/j.addma.2019.05.017>.
- [16] S. Tammam-Williams, P.J. Withers, I. Todd, P.B. Prangnell, The effectiveness of hot isostatic pressing for closing porosity in titanium parts manufactured by selective electron beam melting, *Metall. Mater. Trans. A* 47 (2016) 1939–1946, <https://doi.org/10.1007/s11661-016-3429-3>.
- [17] A. du Plessis, E. Macdonald, Hot isostatic pressing in metal additive manufacturing: X-ray tomography reveals details of pore closure, *Addit. Manuf.* 34 (2020), 101191, <https://doi.org/10.1016/j.addma.2020.101191>.
- [18] H. Ghasemi-Tabasi, J. Jhabvala, E. Boillat, T. Ivas, R. Drissi-Daoudi, R.E. Logé, An effective rule for translating optimal selective laser melting processing parameters from one material to another, *Addit. Manuf.* 36 (2020), 101496, <https://doi.org/10.1016/j.addma.2020.101496>.
- [19] A.A. Martin, N.P. Calta, S.A. Khairallah, J. Wang, P.J. Depond, A.Y. Fong, V. Thampy, G.M. Guss, A.M. Kiss, K.H. Stone, C.J. Tassone, J. Nelson Weker, M. F. Toney, T. van Buuren, M.J. Matthews, Dynamics of pore formation during laser powder bed fusion additive manufacturing, *Nat. Commun.* 10 (1) (2019) 10, <https://doi.org/10.1038/s41467-019-10009-2>.
- [20] G. Kasperovich, J. Haubrich, J. Gussone, G. Requena, Correlation between porosity and processing parameters in TiAl6V4 produced by selective laser melting, *Mater. Des.* 105 (2016) 160–170, <https://doi.org/10.1016/j.matdes.2016.05.070>.
- [21] N.T. Aboulkhair, N.M. Everitt, I. Ashcroft, C. Tuck, Reducing porosity in AlSi10Mg parts processed by selective laser melting, *Addit. Manuf.* 1–4 (2014) 77–86, <https://doi.org/10.1016/j.addma.2014.08.001>.
- [22] C. Zhao, N.D. Parab, X. Li, K. Fezzaa, W. Tan, A.D. Rollett, T. Sun, Critical instability at moving keyhole tip generates porosity in laser melting, *Science* 370 (80-) (2020) 1080–1086, <https://doi.org/10.1126/science.abd1587>.
- [23] Y. Huang, T.G. Fleming, S.J. Clark, S. Marussi, K. Fezzaa, J. Thiyyagalingam, C.L. A. Leung, P.D. Lee, Keyhole fluctuation and pore formation mechanisms during laser powder bed fusion additive manufacturing, *Nat. Commun.* 13 (2022), 1170, <https://doi.org/10.1038/s41467-022-28694-x>.
- [24] Y. Chen, S.J. Clark, C.L.A. Leung, L. Sinclair, S. Marussi, M.P. Olbinado, E. Boller, A. Rack, I. Todd, P.D. Lee, In-situ Synchrotron imaging of keyhole mode multi-layer laser powder bed fusion additive manufacturing, *Appl. Mater. Today* 20 (2020), 100650, <https://doi.org/10.1016/j.apmt.2020.100650>.
- [25] R. Fabbro, Scaling laws for the laser welding process in keyhole mode, *J. Mater. Process. Technol.* 264 (2019) 346–351, <https://doi.org/10.1016/j.jmatprotec.2018.09.027>.
- [26] Z. Gan, O.L. Kafka, N. Parab, C. Zhao, L. Fang, O. Heinonen, T. Sun, W.K. Liu, Universal scaling laws of keyhole stability and porosity in 3D printing of metals, *Nat. Commun.* 12 (2021), <https://doi.org/10.1038/s41467-021-22704-0>.
- [27] R. Cunningham, C. Zhao, N. Parab, C. Kantzos, J. Pauza, K. Fezzaa, T. Sun, A. D. Rollett, Keyhole threshold and morphology in laser melting revealed by ultrahigh-speed x-ray imaging, *Science* 363 (80-) (2019) 849–852, <https://doi.org/10.1126/science.aav4687>.
- [28] L. Wang, Y. Zhang, H.Y. Chia, W. Yan, Mechanism of keyhole pore formation in metal additive manufacturing, *Npj Comput. Mater.* 8 (2022), 22, <https://doi.org/10.1038/s41524-022-00699-6>.
- [29] N. Sanaei, A. Fatemi, Defects in additive manufactured metals and their effect on fatigue performance: a state-of-the-art review, *Prog. Mater. Sci.* 117 (2021), 100724, <https://doi.org/10.1016/j.pmatsci.2020.100724>.
- [30] B. Zhang, Y. Li, Q. Bai, Defect formation mechanisms in selective laser melting: a review, *Chin. J. Mech. Eng.* 30 (2017) 515–527, <https://doi.org/10.1007/s10033-017-0121-5>.
- [31] M. Hamidi Nasab, G. Masinelli, C. de Formanoir, L. Schlenger, S. Van Petegem, R. Esmaeilzadeh, K. Wasmer, A. Ganvir, A. Salminen, F. Aymanns, F. Marone, V. Pandiyan, S. Goel, R.E. Logé, Operando X-Ray imaging of stochastic inter-regime instabilities in laser melting processes: direct evidence of acoustic emission signatures, *Res. Sq.* (2023), <https://doi.org/10.21203/rs.3.rs-2607808/v1>.
- [32] K. Wei, M. Lv, X. Zeng, Z. Xiao, G. Huang, M. Liu, J. Deng, Effect of laser remelting on deposition quality, residual stress, microstructure, and mechanical property of selective laser melting processed Ti-5Al-2.5Sn alloy, *Mater. Charact.* 150 (2019) 67–77, <https://doi.org/10.1016/j.matchar.2019.02.010>.
- [33] J. Guan, Q. Wang, The effect of a remelting treatment scanning strategy on the surface morphology, defect reduction mechanism, and mechanical properties of a selective laser-melted Al-based alloy, *J. Mater. Sci.* (2022), <https://doi.org/10.1007/s10853-021-06761-w>.
- [34] W. Yu, S.L. Sing, C.K. Chua, X. Tian, Influence of re-melting on surface roughness and porosity of AlSi10Mg parts fabricated by selective laser melting, *J. Alloy. Compd.* 792 (2019) 574–581, <https://doi.org/10.1016/j.jallcom.2019.04.017>.
- [35] E. Yasa, J. Deckers, J. Kruth, The investigation of the influence of laser re-melting on density, surface quality and microstructure of selective laser melting parts, *Rapid Prototyp. J.* 17 (2011) 312–327, <https://doi.org/10.1080/13552541111156450>.
- [36] S.M.H. Hojjatzadeh, N.D. Parab, W. Yan, Q. Guo, L. Xiong, C. Zhao, M. Qu, L. I. Escano, X. Xiao, K. Fezzaa, W. Everhart, T. Sun, L. Chen, Pore elimination mechanisms during 3D printing of metals, *Nat. Commun.* 10 (2019), 3088, <https://doi.org/10.1038/s41467-019-10973-9>.
- [37] A.M. Kiss, A.Y. Fong, N.P. Calta, V. Thampy, A.A. Martin, P.J. Depond, J. Wang, M. J. Matthews, R.T. Ott, C.J. Tassone, K.H. Stone, M.J. Kramer, A. Van Buuren, M. F. Toney, J.N. Weker, Laser-induced keyhole defect dynamics during metal additive manufacturing, *Adv. Eng. Mater.* 21 (2019), 1900455, <https://doi.org/10.1002/adem.201900455>.
- [38] J. Metelkova, Y. Kinds, K. Kempen, C. de Formanoir, A. Witvrouw, B. Van Hooreweder, On the influence of laser defocusing in Selective Laser Melting of 316L, *Addit. Manuf.* 23 (2018) 161–169, <https://doi.org/10.1016/j.addma.2018.08.006>.
- [39] S. Patel, H. Chen, M. Vlasea, Y. Zou, The influence of divergent laser beams on the laser powder bed fusion of a high reflectivity aluminium alloy, *ArXiv:2105.07920 [Cond-Mat, Physics:Physics]* (2021). <http://arxiv.org/abs/2105.07920>.
- [40] S. Tammam-Williams, H. Zhao, F. Léonard, F. Derguti, I. Todd, P.B. Prangnell, XCT analysis of the influence of melt strategies on defect population in Ti-6Al-4V components manufactured by Selective Electron Beam Melting, *Mater. Charact.* 102 (2015) 47–61, <https://doi.org/10.1016/j.matchar.2015.02.008>.
- [41] S. Berumen, F. Bechmann, S. Lindner, J.P. Kruth, T. Craeghs, Quality control of laser- and powder bed-based Additive Manufacturing (AM) technologies, *Phys. Procedia* 5 (2010) 617–622, <https://doi.org/10.1016/j.phpro.2010.08.089>.
- [42] S. Clijsters, T. Craeghs, S. Buls, K. Kempen, J.P. Kruth, In situ quality control of the selective laser melting process using a high-speed, real-time melt pool monitoring system, *Int. J. Adv. Manuf. Technol.* 75 (2014) 1089–1101, <https://doi.org/10.1007/s00170-014-6214-8>.
- [43] S. Shevchik, T. Le-Quang, B. Meylan, F.V. Farahani, M.P. Olbinado, A. Rack, G. Masinelli, C. Leinenbach, K. Wasmer, Supervised deep learning for real-time quality monitoring of laser welding with X-ray radiographic guidance, *Sci. Rep.* 10 (2020), 3389, <https://doi.org/10.1038/s41598-020-60294-x>.
- [44] M. Pavlov, M. Doubenskaia, I. Smurov, Pyrometric analysis of thermal processes in SLM technology, *Phys. Procedia* 5 (2010) 523–531, <https://doi.org/10.1016/J.PHPRO.2010.08.080>.

- [45] M. Doubenskaia, M. Pavlov, Y. Chivel, Optical system for on-line monitoring and temperature control in selective laser melting technology, *Key Eng. Mater.* 437 (2010) 458–461, <https://doi.org/10.4028/www.scientific.net/KEM.437.458>.
- [46] T. Furumoto, T. Ueda, M.R. Alkahari, A. Hosokawa, Investigation of laser consolidation process for metal powder by two-color pyrometer and high-speed video camera, *CIRP Ann.* 62 (2013) 223–226, <https://doi.org/10.1016/j.cirp.2013.03.032>.
- [47] J.-B. Forien, N.P. Calta, P.J. Depond, G.M. Guss, T.T. Roehling, M.J. Matthews, Detecting keyhole pore defects and monitoring process signatures during laser powder bed fusion: a correlation between in situ pyrometry and ex situ X-ray radiography, *Addit. Manuf.* (2020), 101336.
- [48] A. Gaikwad, B. Giera, G.M. Guss, J.B. Forien, M.J. Matthews, P. Rao, Heterogeneous sensing and scientific machine learning for quality assurance in laser powder bed fusion – a single-track study, *Addit. Manuf.* 36 (2020), 101659, <https://doi.org/10.1016/j.addma.2020.101659>.
- [49] T.G. Spears, S.A. Gold, In-process sensing in selective laser melting (SLM) additive manufacturing, *Integr. Mater. Manuf. Innov.* 5 (2016) 16–40, <https://doi.org/10.1186/s40192-016-0045-4>.
- [50] T. Furumoto, M.R. Alkahari, T. Ueda, M.S.A. Aziz, A. Hosokawa, Monitoring of laser consolidation process of metal powder with high speed video camera, *Phys. Procedia* 39 (2012) 760–766, <https://doi.org/10.1016/j.phpro.2012.10.098>.
- [51] S.K. Everton, M. Hirsch, P.I. Stavroulakis, R.K. Leach, A.T. Clare, Review of in-situ process monitoring and in-situ metrology for metal additive manufacturing, *Mater. Des.* 95 (2016) 431–445, <https://doi.org/10.1016/j.matdes.2016.01.099>.
- [52] L. Li, W.M. Steen, Non-contact acoustic emission monitoring during laser processing, *LIA (Laser Inst. Am.)* 75 (1993) 719–728, <https://doi.org/10.2351/1.5058543>.
- [53] Y. Mao, G. Kinsman, W.W. Duley, Real-time fast fourier transform analysis of acoustic emission during CO₂ laser welding of materials, *J. Laser Appl.* 5 (1993) 17–22, <https://doi.org/10.2351/1.4745326>.
- [54] W.W. Duley, Y.L. Mao, The effect of surface condition on acoustic emission during welding of aluminium with CO₂ laser radiation, *J. Phys. D. Appl. Phys.* 27 (1994) 1379–1383, <https://doi.org/10.1088/0022-3727/27/7/007>.
- [55] D. Farson, K. Hillsley, J. Sames, Frequency-time characteristics of air-borne signals from laser welds, *J. Laser Appl.* 8 (1996) 33–42.
- [56] V. Pandiyan, G. Masinelli, C. Navarre, T. Le-Quang, M. Hamidi Nasab, C. de Formanoir, R. Esmailzadeh, S. Goel, F. Marone, R.E. Logé, S. Van Petegem, K. Wasmer, Deep learning-based monitoring of laser powder bed fusion process on variable time-scales using heterogeneous sensing and operando X-ray radiography guidance, *Addit. Manuf.* 58 (2022), 103007.
- [57] R. Drissi-Daoudi, G. Masinelli, C. de Formanoir, K. Wasmer, J. Jhavalva, R.E. Logé, Acoustic emission for the prediction of processing regimes in Laser Powder Bed Fusion, and the generation of processing maps, *Addit. Manuf.* 67 (2023), 103484.
- [58] J.R. Tempelman, A.J. Wachtor, E.B. Flynn, P.J. Depond, J.-B. Forien, G.M. Guss, N. P. Calta, M.J. Matthews, Detection of keyhole pore formations in laser powder-bed fusion using acoustic process monitoring measurements, *Addit. Manuf.* (2022), 102735, <https://doi.org/10.1016/j.addma.2022.102735>.
- [59] K. Ito, M. Kusano, M. Memura, M. Watanabe, Detection and location of microdefects during selective laser melting by wireless acoustic emission measurement, *Addit. Manuf.* 40 (2021), 101915, <https://doi.org/10.1016/j.addma.2021.101915>.
- [60] R. Drissi-Daoudi, V. Pandiyan, R. Logé, S. Shevchik, G. Masinelli, H. Ghasemi-Tabasi, A. Parrilli, K. Wasmer, Differentiation of materials and laser powder bed fusion processing regimes from airborne acoustic emission combined with machine learning, *Virtual Phys. Prototyp.* 17 (2022) 181–204, <https://doi.org/10.1080/17452759.2022.2028380>.
- [61] V. Pandiyan, R. Drissi-Daoudi, S. Shevchik, G. Masinelli, T. Le-Quang, R. Logé, K. Wasmer, Semi-supervised Monitoring of Laser powder bed fusion process based on acoustic emissions, *Virtual Phys. Prototyp.* 16 (2021) 481–497, <https://doi.org/10.1080/17452759.2021.1966166>.
- [62] V. Pandiyan, R. Drissi-Daoudi, S. Shevchik, G. Masinelli, R. Logé, K. Wasmer, Analysis of time, frequency and time-frequency domain features from acoustic emissions during Laser Powder-Bed fusion process, *Procedia CIRP* 94 (2020) 392–397, <https://doi.org/10.1016/j.procir.2020.09.152>.
- [63] N. Eschner, L. Weiser, B. Häfner, G. Lanza, Classification of specimen density in Laser Powder Bed Fusion (L-PBF) using in-process structure-borne acoustic process emissions, *Addit. Manuf.* 34 (2020), 101324, <https://doi.org/10.1016/j.addma.2020.101324>.
- [64] K. Wasmer, T. Le-Quang, B. Meylan, F. Vakili-Farahani, M.P. Olbinado, A. Rack, S. A. Shevchik, Laser processing quality monitoring by combining acoustic emission and machine learning: a high-speed X-ray imaging approach, *Procedia CIRP* 74 (2018) 654–658, <https://doi.org/10.1016/j.procir.2018.08.054>.
- [65] S.A. Shevchik, C. Kenel, C. Leinenbach, K. Wasmer, Acoustic emission for in situ quality monitoring in additive manufacturing using spectral convolutional neural networks, *Addit. Manuf.* 21 (2018) 598–604, <https://doi.org/10.1016/j.addma.2017.11.012>.
- [66] Q. Guo, C. Zhao, M. Qu, L. Xiong, L.I. Escano, S.M.H. Hojjatzadeh, N.D. Parab, K. Fezzaa, W. Everhart, T. Sun, L. Chen, In-situ characterization and quantification of melt pool variation under constant input energy density in laser powder bed fusion additive manufacturing process, *Addit. Manuf.* 28 (2019) 600–609, <https://doi.org/10.1016/j.addma.2019.04.021>.
- [67] N. Kouraytem, X. Li, R. Cunningham, C. Zhao, N. Parab, T. Sun, A.D. Rollett, A. D. Spear, W. Tan, Effect of laser-matter interaction on molten pool flow and keyhole dynamics, *Phys. Rev. Appl.* 11 (2019) 1, <https://doi.org/10.1103/PhysRevApplied.11.064054>.
- [68] A.A. Martin, N.P. Calta, S.A. Khairallah, J. Wang, P.J. Depond, A.Y. Fong, V. Thampy, G.M. Guss, A.M. Kiss, K.H. Stone, C.J. Tassone, J. Nelson Weker, M. F. Toney, T. van Buuren, M.J. Matthews, Dynamics of pore formation during laser powder bed fusion additive manufacturing, *Nat. Commun.* 10 (2019), 1987, <https://doi.org/10.1038/s41467-019-10009-2>.
- [69] C. Zhao, Q. Guo, X. Li, N. Parab, K. Fezzaa, W. Tan, L. Chen, T. Sun, Bulk-explosion-induced metal spattering during laser processing, *Phys. Rev. X* 9 (2019) 21052, <https://doi.org/10.1103/PhysRevX.9.021052>.
- [70] N.D. Parab, C. Zhao, R. Cunningham, L.I. Escano, K. Fezzaa, W. Everhart, A. D. Rollett, L. Chen, T. Sun, Ultrafast X-ray imaging of laser–metal additive manufacturing processes, *J. Synchrotron Radiat.* 25 (2018) 1467–1477, <https://doi.org/10.1107/S1600577518009554>.
- [71] Q. Guo, C. Zhao, L.I. Escano, Z. Young, L. Xiong, K. Fezzaa, W. Everhart, B. Brown, T. Sun, L. Chen, Transient dynamics of powder spattering in laser powder bed fusion additive manufacturing process revealed by in-situ high-speed high-energy X-ray imaging, *Acta Mater.* 151 (2018) 169–180, <https://doi.org/10.1016/j.actamat.2018.03.036>.
- [72] C.L.A. Leung, S. Marussi, M. Towrie, J. del Val Garcia, R.C. Atwood, A.J. Bodey, J. R. Jones, P.J. Withers, P.D. Lee, Laser-metal interactions in additive manufacturing of stainless steel SS316L and 13-93 bioactive glass revealed by in situ X-ray imaging, *Addit. Manuf.* 24 (2018) 647–657, <https://doi.org/10.1016/j.addma.2018.08.025>.
- [73] C. Zhao, K. Fezzaa, R.W. Cunningham, H. Wen, F. De Carlo, L. Chen, A.D. Rollett, T. Sun, Real-time monitoring of laser powder bed fusion process using high-speed X-ray imaging and diffraction, *Sci. Rep.* (2017), <https://doi.org/10.1038/s41598-017-03761-2>.
- [74] N.P. Calta, J. Wang, A.M. Kiss, A.A. Martin, P.J. Depond, G.M. Guss, V. Thampy, A. Y. Fong, J.N. Weker, K.H. Stone, C.J. Tassone, M.J. Kramer, M.F. Toney, A. Van Buuren, M.J. Matthews, An instrument for in situ time-resolved X-ray imaging and diffraction of laser powder bed fusion additive manufacturing processes, *Rev. Sci. Instrum.* 89 (2018) 1–8, <https://doi.org/10.1063/1.5017236>.
- [75] C.L.A. Leung, S. Marussi, R.C. Atwood, M. Towrie, P.J. Withers, P.D. Lee, In situ X-ray imaging of defect and molten pool dynamics in laser additive manufacturing, *Nat. Commun.* (2018), <https://doi.org/10.1038/s41467-018-03734-7>.
- [76] Q. Guo, M. Qu, L.I. Escano, S.M.H. Hojjatzadeh, Z. Young, K. Fezzaa, L. Chen, Revealing melt flow instabilities in laser powder bed fusion additive manufacturing of aluminum alloy via in-situ high-speed X-ray imaging, *Int. J. Mach. Tools Manuf.* 175 (2022), 103861, <https://doi.org/10.1016/j.ijmactools.2022.103861>.
- [77] A.A. Martin, J. Wang, P.J. Depond, M. Strantz, J.-B. Forien, S. Gorgannejad, G. M. Guss, V. Thampy, A.Y. Fong, J.N. Weker, K.H. Stone, C.J. Tassone, M. J. Matthews, N.P. Calta, A laser powder bed fusion system for operando synchrotron x-ray imaging and correlative diagnostic experiments at the Stanford Synchrotron Radiation Lightsource, *Rev. Sci. Instrum.* 93 (2022), 043702, <https://doi.org/10.1063/5.0080724>.
- [78] Y. Chen, S.J. Clark, C.L.A. Leung, L. Sinclair, S. Marussi, M.P. Olbinado, E. Boller, A. Rack, I. Todd, P.D. Lee, In-situ Synchrotron imaging of keyhole mode multi-layer laser powder bed fusion additive manufacturing, *Appl. Mater. Today* 20 (2020), 100650, <https://doi.org/10.1016/j.apmt.2020.100650>.
- [79] L. Sinclair, C.L.A. Leung, S. Marussi, S.J. Clark, Y. Chen, M.P. Olbinado, A. Rack, J. Gardy, G.J. Baxter, P.D. Lee, In situ radiographic and ex situ tomographic analysis of pore interactions during multilayer builds in laser powder bed fusion, *Addit. Manuf.* 36 (2020), 101512, <https://doi.org/10.1016/j.addma.2020.101512>.
- [80] A.A. Martin, N.P. Calta, J.A. Hammons, S.A. Khairallah, M.H. Nielsen, R. M. Shuttlesworth, N. Sinclair, M.J. Matthews, J.R. Jeffries, T.M. Willey, J.R.I. Lee, Ultrafast dynamics of laser-metal interactions in additive manufacturing alloys captured by in situ X-ray imaging, *Mater. Today Adv.* 1 (2019), 100002, <https://doi.org/10.1016/j.mtadv.2019.01.001>.
- [81] C.L.A. Leung, S. Marussi, M. Towrie, R.C. Atwood, P.J. Withers, P.D. Lee, The effect of powder oxidation on defect formation in laser additive manufacturing, *Acta Mater.* (2019), <https://doi.org/10.1016/j.actamat.2018.12.027>.
- [82] R. Cunningham, C. Zhao, N. Parab, C. Kantzos, J. Pauza, K. Fezzaa, T. Sun, A. D. Rollett, Keyhole threshold and morphology in laser melting revealed by ultrahigh-speed x-ray imaging, *Science* 363 (80-) (2019) 849–852, <https://doi.org/10.1126/science.aav4687>.
- [83] S. Hocine, S. Van Petegem, U. Frommherz, G. Tinti, N. Casati, D. Grolimund, H. Van Swygenhoven, A miniaturized selective laser melting device for operando X-ray diffraction studies, *Addit. Manuf.* 34 (2020), 101194, <https://doi.org/10.1016/j.addma.2020.101194>.
- [84] S. Hocine, H. Van Swygenhoven, S. Van Petegem, C.S.T. Chang, T. Maimaitiylili, G. Tinti, D. Ferreira Sanchez, D. Grolimund, N. Casati, Operando X-ray diffraction during laser 3D printing, *Mater. Today* 34 (2020) 30–40, <https://doi.org/10.1016/J.MATTOD.2019.10.001>.
- [85] M. Bührer, M. Stapanoni, X. Rochet, F. Büchi, J. Eller, F. Marone, High-numerical-aperture microscope optics for time-resolved experiments, *J. Synchrotron Radiat.* 26 (2019) 1161–1172, <https://doi.org/10.1107/S1600577519004119>.
- [86] R. Mokso, C.M. Schlepütz, G. Theidel, H. Billich, E. Schmid, T. Celcer, G. Mikuljan, L. Sala, F. Marone, N. Schlumpf, M. Stapanoni, GigaFROST: the gigabit fast readout system for tomography, *J. Synchrotron Radiat.* 24 (2017) 1250–1259, <https://doi.org/10.1107/S1600577517013522>.
- [87] B. Fischer, W. Rohringer, N. Panzer, S. Hecker, Acoustic process control for laser material processing, *Laser Tech. J.* 14 (2017) 21–25, <https://doi.org/10.1002/latj.201700029>.
- [88] S. Tammam-Williams, P.J. Withers, I. Todd, P.B. Prangnell, The influence of porosity on fatigue crack initiation in additively manufactured titanium components, *Sci. Rep.* 7 (2017), <https://doi.org/10.1038/s41598-017-06504-5>.

- [89] C. de Formanoir, U. Paggi, T. Colebrants, L. Thijs, G. Li, K. Vanmeensel, B. Van Hooreweder, Increasing the productivity of laser powder bed fusion: influence of the hull-bulk strategy on part quality, microstructure and mechanical performance of Ti-6Al-4V, *Addit. Manuf.* 33 (2020), 101129, <https://doi.org/10.1016/j.addma.2020.101129>.
- [90] G. Mohr, S.J. Altenburg, K. Hilgenberg, Effects of inter layer time and build height on resulting properties of 316L stainless steel processed by laser powder bed fusion, *Addit. Manuf.* 32 (2020), 101080, <https://doi.org/10.1016/j.addma.2020.101080>.
- [91] Z. Kuai, Z. Li, B. Liu, W. Liu, S. Yang, Effects of remelting on the surface morphology, microstructure and mechanical properties of AlSi10Mg alloy fabricated by selective laser melting, *Mater. Chem. Phys.* 285 (2022), 125901, <https://doi.org/10.1016/j.matchemphys.2022.125901>.